

# Monitoring and Engineering the Light-to-heat Conversion around Plasmonic Gold Nanoparticles using Ratiometric Nanothermometry

*On taking the first step towards optical excitation driven catalysis at the nanoscale.*

Tjom Arens

Supervisors:

dr. Wiebke Albrecht

dr. Freddy Rabouw

Sander Vonk



**Universiteit Utrecht**

Inorganic Chemistry & Catalysis  
Utrecht University

**AMOLF** physics of  
functional complex matter

Hybrid Nanosystems  
AMOLF

January 31, 2022

## Table of Contents

<b>Abstract.....</b>	<b>3</b>
<b>Introduction .....</b>	<b>4</b>
<b>Theory.....</b>	<b>5</b>
Light-to-heat conversion .....	5
Localized surface plasmon resonance.....	6
Ratiometric nanothermometry .....	8
<b>Experimental .....</b>	<b>10</b>
Nanoparticles .....	10
Particle characterization and sample preparation .....	10
Photoluminescence experiments .....	12
Cathodoluminescence experiments .....	13
<b>Results.....</b>	<b>14</b>
Peak assignment .....	14
Photoluminescence.....	14
Supraparticles.....	14
Gold spheres.....	17
Gold rods.....	19
Cathodoluminescence.....	21
<b>Conclusion .....</b>	<b>25</b>
<b>Outlook .....</b>	<b>26</b>
<b>References:.....</b>	<b>27</b>
<b>Appendix.....</b>	<b>30</b>
1 - Particle analyser + script .....	30
2 - Effect of overlapping $^2H_{9/2}$ and $^4S_{3/2}$ emission .....	33
3 - Electron penetration depth simulations (Casino).....	34

## Abstract

Currently, most catalytic reactions are fossil fuel driven, which makes them unsustainable for future use, and reaching high selectivity's is often a challenge. A possible new way to increase the selectivity and efficiency of these catalytic reactions is the use of optical excitation. Before such catalytic reactions at the nanoscale are possible a method is required that can induce, tune and monitor heating at this scale. In this thesis, we use the excitation of the plasmon resonance of gold nanoparticles to induce and tune local heating, while monitoring the temperature using ratiometric nanothermometry on NaYF<sub>4</sub>:Er<sup>3+</sup> (2%), Yb<sup>3+</sup> (18%) thermometer particles. We developed a method that can induce and tune the temperature of single gold nanoparticles with photoluminescence, while subsequently monitoring the temperature with a micrometer scale resolution. A clear excitation power dependent temperature profile around a single gold nanoparticle was observed with a tunable temperature from room temperature to 95 °C that diminished over a radius of 3µm. We also took the first step in translating this method for photoluminescence to cathodoluminescence, which has the potential to increase the temperature and spatial resolution to the nanometer scale. This work opens up the possibility towards light-to-heat driven catalytic reactions with a micrometer and potentially nanometer scale temperature and spatial resolution.

## Introduction

Nowadays, the wish for sustainable growth in combination with the wish for energy security for future generations plays an important role. Therefore, there are a lot of reasons to limit our society's dependency on fossil fuels.<sup>1</sup> A big proportion of the consumption of fossil fuels is used for driving chemical reactions, which makes them unsustainable for future use. Therefore, more sustainable ways are required to drive such chemical reactions. A new sustainable way for catalytic reactions would be catalysis driven by optical excitation. In this way, catalytic particles can be heated by exciting nearby particles using light.

Particles well known for their efficient light-to-heat conversion are metallic nanoparticles (NPs).<sup>2</sup> Although, originally light-induced heating of metal NPs was considered to be a major weakness as applications were focused on their other unique optical properties, such as the concentration and manipulation of light below the free space diffraction limit and the enhanced light scattering and absorption due to localized plasmon resonances (LSP).<sup>2-4</sup> The last decade, scientists realized that metal NPs could be turned into nano heating-sources and that by tuning the size, shape and dielectric environment of the NPs the spectral properties of the resonances could be engineered.<sup>5</sup> Especially, gold NPs, known for their chemical inertia, easy functionalization, low toxicity and LSP upon illumination in the visible to infrared wavelength range, have received a lot of attention in the field of *thermo-plasmonics*.<sup>5,6</sup> Some interesting applications of thermo-plasmonics are currently in photo-thermal cancer treatment<sup>7</sup>, nano-surgery<sup>8</sup>, drug delivery<sup>9</sup>, and microfluidics<sup>10</sup>. Thermo-plasmonics thus provides a powerful tool with a high level of heat control at the nanoscale<sup>3</sup> and could thus be ideal for driving catalytic reactions using optical excitation at the nanoscale. However, the reshaping of NPs under laser illumination, was observed to occur for temperatures as low as 100 °C.<sup>11,12</sup> When NPs reshape this will also change their optical and hence heating properties. Therefore, constant monitoring of the temperature is required. Currently, several techniques are being used to determine the temperature of plasmonic NPs: fluorescence polarization anisotropy (FPA)<sup>13</sup>, magnetic resonance imaging (MRI)<sup>7</sup>, cross-grating phase microscopy<sup>14</sup> and time-resolved-anti-stokes photoluminescence<sup>15</sup>. None of these techniques is however viable for measuring a temperature profile around a NP without being dissolved into a liquid, while being cheap and practical. A well-known temperature measurement technique that is not limited by the above is ratiometric nanothermometry.<sup>16</sup>

In this thesis, we developed a new method to subsequently heat and monitor the temperature around a single gold NP with the goal to eventually be able to perform catalytic reactions at the nanoscale driven by optical excitation. We used ratiometric nanothermometry to monitor the temperature of a monolayer of thermometer particles, NaYF<sub>4</sub>:Er<sup>3+</sup> (2%), Yb<sup>3+</sup> (18%), while subsequently heating a single gold NP (sphere, rod or supraparticles) due to excitation at its resonance.<sup>17</sup> Because each thermometer particle can function as a heat sensor, high spatial resolution can be acquired. Luminescence was collected using either photoluminescence (PL) or cathodoluminescence (CL) and the temperature was calculated from the respective emission spectra.<sup>18-22</sup> PL was bound to the diffraction limit of light and could therefore hardly reach sub micrometer spatial resolution, while CL can potentially reach higher spatial resolutions. In this thesis, we will first discuss some theory on thermo-plasmonics and ratiometric nanothermometry. Then we will discuss our method for micrometer scale resolution temperature measurements using PL, while showing the measured temperature profiles for single gold NPs with different shapes and optical

excitations. Finally, we attempt to translate this method to CL measurements and discuss the current limitations and possible solutions of this technique.

## Theory

### Light-to-heat conversion

The first step in the excitation of an electron, and the formation of hot carriers, is the absorption of a photon. Electrons in a metallic NP move freely and can be periodically displaced with respect to the lattice ion due to the electric field of an incoming photon. This displacement results in charges at opposite surfaces and will set up an electric field, which will tend to restore charge neutrality (Fig. 1a). The electrons will therefore acquire momentum from the field and overshoot the equilibrium configuration. This results in a collective electron oscillation called a plasma oscillation, with a plasma frequency determined by the restoring force and effective mass of the electron.<sup>23</sup> However, in a system that is sufficiently small, electrons will ‘feel’ the presence of boundaries and will therefore modify their collective behavior accordingly.<sup>24</sup> The resonance frequency of these LSPs is strongly dependent on the dielectric environment, the size and the shape of the metallic NP.<sup>3</sup> Upon illumination of these LSP resonances an antenna effect is produced resulting in light collection over an area larger than the physical size of the NP thereby enhancing light absorption (Fig. 1a).<sup>24,25</sup> The excited LSP resonance, by the absorption of a photon, can be damped either radiatively or non-radiatively through the re-emission of a photon or the creation of hot electron-hole pairs via Landau damping (Fig. 1b). In Landau damping a SP is transferred forming a single hot electron-hole pair. A possible population distribution after Landau damping is shown in figure 2b.<sup>26</sup> The energy of these hot carriers is quickly redistributed to lower energy electrons via electron-electron scattering processes. When the energy of a hot carrier has sufficiently decreased, it can couple to the lattice through electron-phonon coupling.<sup>27</sup> An equilibrium temperature with the lattice will eventually be reached that is best described via the two-temperature model (Fig. 1c).<sup>28</sup> During a final step this heat dissipates through particle-medium interfaces. The rate of this heat dissipation is dependent on the medium, particle size and laser source (Fig. 1d).<sup>29</sup> Note that only this final step can be measured during our heating experiments.

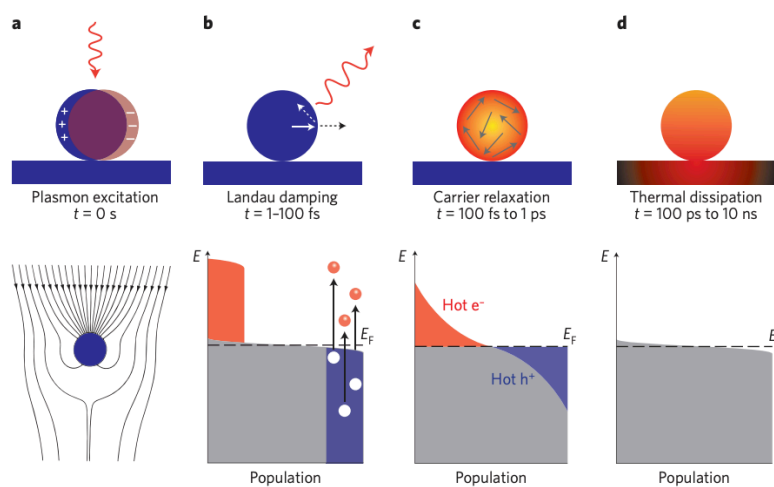


*Figure 1:* a) Excitation of a metallic NP plasmon due to the electric field of an incoming electron. b) Damping of the LSP resonance due to emission of a photon or by the creation of a hot electron-hole pair via Landau damping with a possible population distribution after this damping. c) Hot carriers quickly redistribute their energy to lower energy electrons via electron-electron scattering processes. d) Heat dissipation through particle-medium interface. Image taken from reference 25.

## Localized surface plasmon resonance

The LSP resonance frequency of metallic NPs is strongly dependent on the dielectric environment, the size and the shape of the particle. This enables tuning of the LSP resonance from the visible to the near-infrared wavelength range for noble metals, such as gold, silver or copper.<sup>30</sup> A metallic sphere that is much smaller than the excitation wavelength ( $ka \ll 1$ ) can be considered a source of electromagnetic dipole radiation when driven by an external electric field, according to the so-called quasistatic approximation. In this case, a simple closed-form expression can be derived for the origin of the LSP resonances. The polarizability of a sphere is given by:<sup>30</sup>

$$\alpha = 3V\varepsilon_s \frac{\varepsilon(\omega) - \varepsilon_s}{\varepsilon(\omega) + 2\varepsilon_s} \quad [1]$$

With  $V$  the volume of the sphere,  $\varepsilon(\omega)$  the frequency-dependent dielectric constant of the sphere and  $\varepsilon_s$  the dielectric constant of the environment. A resonance occurs at the maximum of the polarizability and thus when  $\varepsilon(\omega) \approx -2\varepsilon_s$ . However, for larger spheres this is no longer valid as the charges in the nanoparticle no longer oscillate uniformly with the electric field, resulting in a phase delay over the particle. This effect is called the retardation effect.<sup>3</sup>

Directly related to the polarizability, which we can measure during our experiments, are the optical cross sections. These cross sections are defined as such that absorbed and scattered energies can be calculated by multiplication with the light irradiance  $I$  [ $\text{W m}^{-2}$ ]. Optical cross section can be defined for any particle that interacts with light and are given by:<sup>30</sup>

$$\sigma_{\text{sca}} = \frac{k^4}{6\pi} |\alpha|^2 \quad [2]$$

$$\sigma_{\text{ext}} = k\text{Im}(\alpha) \quad [3]$$

$$\sigma_{\text{abs}} = \sigma_{\text{ext}} - \sigma_{\text{sca}} \quad [4]$$

For small spheres ( $< 40$  nm) it can be assumed that  $\sigma_{\text{abs}} \approx \sigma_{\text{ext}} = k\text{Im}(\alpha)$  as  $\sigma_{\text{sca}}$  scales with  $V^2$ , while  $\sigma_{\text{ext}}$  scales with  $V$  and will thus change much faster. Therefore, it can be expected that absorption is dominant for smaller NPs, while for bigger NPs scattering dominates. The light-to-heat conversion efficiency, or photothermal efficiency, is thus also expected to be higher for smaller particles. Experimental work by Jiang et al.<sup>29</sup> has verified these theoretical assumptions. Knowing the absorption and scattering cross section, the absorbed and scattered power by the NP can be expressed as:<sup>30</sup>

$$P_{\text{abs}} = \sigma_{\text{abs}} I \quad [5]$$

$$P_{\text{sca}} = \sigma_{\text{sca}} I \quad [6]$$

The irradiance of a focused Gaussian beam is given by:

$$I = \frac{P}{\pi\sigma^2} \quad [7]$$

where  $P$  is the power of the laser,  $\sigma$  is the standard deviation, approximately equal to  $\lambda/2NA$  ( $NA$  is the numerical aperture of the microscope objective).

With the absorbed power by the particle the temperature distribution inside the particle, in the steady state regime, can then be calculated using the thermal diffusion equation:<sup>3</sup>

$$\nabla \cdot [k(r)\nabla T(r)] = -P_{abs}(r) \text{ inside the NP} \quad [8]$$

With  $T(r)$  the temperature distribution as a result of an external heating source of power density  $P_{abs}(r)$  and a position dependent, thermal conductivity  $k(r)$ . For the case of a spherical gold particle the thermal diffusion equation can be solved to:<sup>31</sup>

$$\Delta T(r) = \Delta T_{NP} \frac{R}{r} \text{ for } r > R \quad [9]$$

Where  $\Delta T_{NP}$  is the temperature change in the NP as a result of the absorbed power  $P_{abs}$ . Although,  $P_{abs}$  is non-uniform, the temperature in the particle can be considered uniform due to the high thermal conductivity with respect to the surroundings.<sup>31</sup> Therefore, the heating of the gold NP and its surroundings is directly related to the absorbed power by the NP, which in its turn is related to the absorption cross section and the irradiance.

During our experiments the irradiance can be easily tuned by changing the power of the laser, the absorption cross section however cannot be changed during an experiment as it is dependent on the nature, size, shape, and dielectric environment of the metallic NP.<sup>5</sup> To easily tune the heating of our gold NP during an experiment it is therefore important to match the illumination wavelength with the wavelength of the LPR to maximize the absorption cross section. Hereby, we only need to change the power of the laser to drastically change the local temperature around the illuminated NP.

When the size of the NP is increased the plasmonic resonance redshifts (Fig. 2). This is because the quasistatic approximation is no longer valid as the electric field within the particle has a different phase throughout the particle. The plasmon resonances of spherical particles can be derived using Mie theory and different shaped particles solving the full Maxwell equations.<sup>32,33</sup>

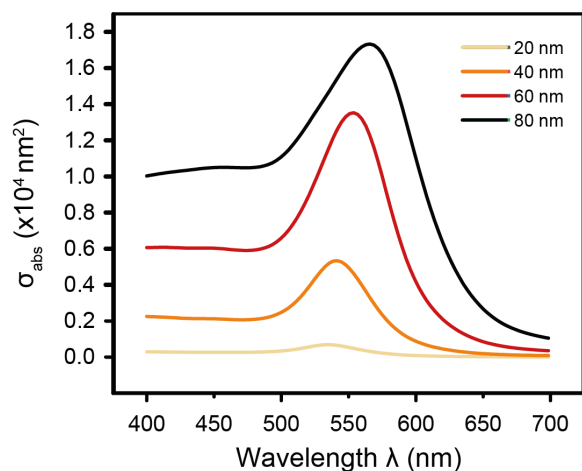


Figure 2: Calculated scattering spectrum using the full Maxwell equations, for spherical gold nanoparticles with a radius of 20, 40, 60 or 80 nm and  $n_s = 1.51$ .

Although, the plasmon resonance can be redshifted by increasing the particles size it is not the most efficient way of doing so as the plasmon resonance can be hardly shifted above 600 nm for spherical particles. A better way to redshift the plasmon resonance is by changing the aspect ratio (AR) of the NPs and illuminating the rods with a polarization along their longitudinal axis (Fig. 3a). Not only does this asymmetry result in a significant redshift of the plasmon resonance it also strongly enhances the amplitude.<sup>30</sup> As the plasmon resonance occurs when  $\varepsilon(\omega) \approx -2\varepsilon_s$  where  $\varepsilon_s = n_s^2$ , the position and amplitude of the resonance are also strongly related to the refractive index of the surrounding medium. A third option to tune the plasmon resonance is therefore changing the refractive index of the surrounding medium (Fig. 3b). Note however, that for comparison of the effect of the surrounding medium a constant irradiance  $I$  should be used as the electric field itself depends on the refractive index of the surroundings.<sup>30</sup>

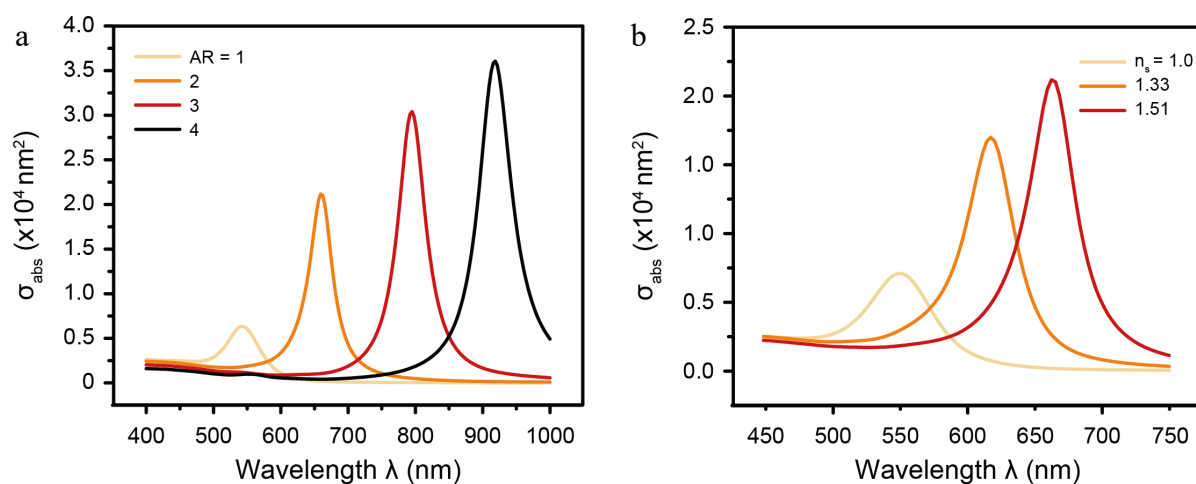


Figure 3: Calculated scattering spectrum using the full Maxwell equations, for rod-shaped gold nanoparticles a) with different aspect ratio (AR) and similar volumes the dimension of the rods are 42 x 42, 30 x 60, 25x75, 21 x 84 nm and  $n_s = 1.51$ . b) with dimensions of 30 x 60 nm and different  $n_s$  of 1, 1.33 or 1.51.

### Ratiometric nanothermometry

To monitor the temperature around plasmonic gold particles, during our experiments, ratiometric nanothermometry is used. This technique uses the temperature dependent luminescence intensity ratio between two thermally coupled energy levels of a certain lanthanide ion as a measure for the temperature.<sup>17</sup> The valance electrons of the lanthanide series are positioned in the 4f orbitals. Within the 4f-orbitals the electrons can redistribute themselves upon illumination with light, these transitions are known as intraconfigurational f-f transitions. These intraconfigurational f-f transitions are parity forbidden resulting in long excited state lifetimes. Furthermore, because the 4f-orbitals are shielded by the more outlying filled 5s and 5p orbitals, these electrons are relatively insensitive to the surroundings resulting in the characteristic narrow emission lines.<sup>34</sup> Some of these lanthanide ions have energy levels that are so close together that thermal energy is sufficient for fast relaxation between two levels.<sup>35</sup> The population in these states is temperature dependent and can be used to determine the temperature by measuring the relative emission intensity from the two energy levels.

In this study we use thermometer particles consisting of  $\text{NaYF}_4$  doped with the lanthanide ions erbium ( $\text{Er}^{3+}$ ) and ytterbium ( $\text{Yb}^{3+}$ ). Upon infrared excitation of ytterbium, characteristic



green luminescence of erbium is observed as the result of an upconversion (UC) process. The major processes in this energy transfer up conversion (ETU) are depicted in figure 4. The majority of light absorption is by ytterbium due to a higher doping concentration and higher absorption cross-section.<sup>36</sup> When a near-infrared photon is absorbed by ytterbium an electron can be excited to the  $^2F_{5/2}$  excited state via an intraconfigurational f-f transition. The excited ytterbium ion can then transfer its energy to the erbium excited state,  $^4I_{11/2}$ , via the Förster energy transfer process.<sup>37</sup> In this process relaxation of the excited ytterbium ion occurs simultaneously with excitation of erbium to the excited state.<sup>38</sup> When this process occurs again during the excited state lifetime of erbium, it is further excited to the  $^4F_{7/2}$  excited state, from which it rapidly decays non-radiatively to the  $^2H_{11/2}$  and  $^4S_{3/2}$  excited state followed by radiative decay to the ground state.<sup>37</sup>

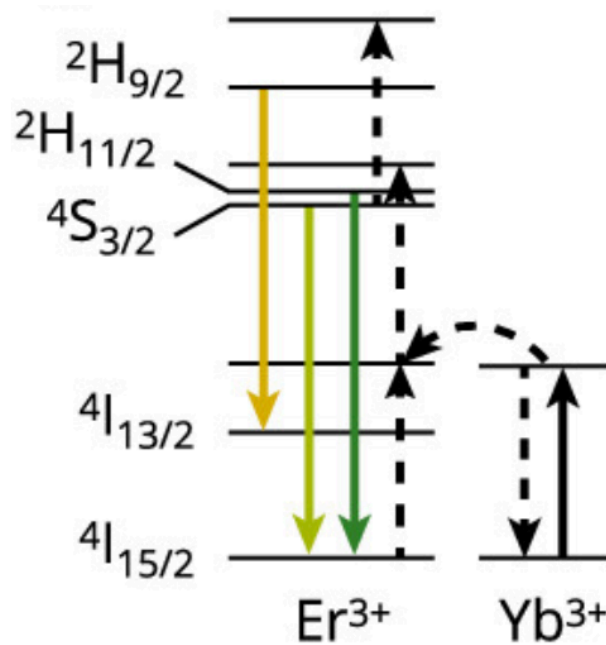


Figure 4: Simplified energy level diagram for the important emissions (colored arrows), absorptions (black arrow), and energy transfers (dashed arrow) in the  $NaYF_4:Er^{3+}$  (2%),  $Yb^{3+}$  (18%) thermometer particles. Image taken from reference 37.

The  $^2H_{11/2}$  and  $^4S_{3/2}$  excited state of erbium are thermally coupled as the energy gap between the two states is similar to the thermal energy at room temperature ( $600\text{ cm}^{-1} = \pm 3k_B T$ ).<sup>39</sup> The population in the two levels can be redistributed, via Boltzmann statistics, due to thermal energy. In a steady state condition, the population of the higher energy state,  $^2H_{11/2}$ , is given by:<sup>17</sup>

$$N_{2H_{11/2}} = N_{4S_{3/2}} e^{-\frac{\Delta E}{k_B T}} \quad [10]$$

With  $N_{2H_{11/2}}$  and  $N_{4S_{3/2}}$  the population in the respective energy level,  $\Delta E$  the energy gap between the two states,  $k_B$  the Boltzmann constant and  $T$  the temperature. Since both states are populated and the emission intensity is proportional to the population in the respective state, both states will contribute to the emission spectrum. The emission intensity  $I$  from the excited level to the ground state is then given by:<sup>17</sup>

$$I_i = \varphi_i N_i \quad [11]$$

With  $\varphi_i$  being a constant dependent on a variety of geometrical factors and on intrinsic properties of the emitting level, such as the spontaneous emission rate. The Boltzmann equation can then be derived by combining equation ... and ...to:<sup>17</sup>

$$\frac{I_{2H_{11/2}}}{I_{4S_{3/2}}} = \frac{\varphi_{2H_{11/2}}}{\varphi_{4S_{3/2}}} \frac{N_{2H_{11/2}}}{N_{4S_{3/2}}} = \frac{\varphi_{2H_{11/2}}}{\varphi_{4S_{3/2}}} e^{-\frac{\Delta E}{k_B T}} \quad [12]$$

Replacing the constant term  $\frac{\varphi_{2H_{11/2}}}{\varphi_{4S_{3/2}}}$  with  $C$  gives the following relationship between,  $\Delta E$ , the temperature and the luminescence intensity peak ratio of the thermally coupled states:

$$\frac{I_{2H_{11/2}}}{I_{4S_{3/2}}} = C e^{-\frac{\Delta E}{k_B T}} \quad [13]$$

Thus, the temperature can be calculated using a temperature calibration and experimental values for the luminescence intensity peak ratio.

## Experimental

### Nanoparticles

The thermometer particles were obtained from René Moesbergen and synthesized according to the method described by Geitenbeek et al.<sup>19</sup> The synthesis consists of two steps: nucleation and growth. In the nucleation step small nuclei of cubic NaYF<sub>4</sub>: Er<sup>3+</sup>, Yb<sup>3+</sup> are formed by adding Ln(Ac)<sub>3</sub> with an Y : Yb : Er ratio of 80 : 18 : 2 to a mixture of oleic acid and 1-octadecene. Followed by the addition of NaOH (in MeOH) and NH<sub>4</sub>F (in MeOH). The growth of the small cubic NaYF<sub>4</sub>: Er<sup>3+</sup>, Yb<sup>3+</sup> particles to form larger hexagonal nanoparticles is then initiated by heating the reaction mixture. Mistakes were made during the growth step of one of the syntheses resulting in a batch of significantly smaller particles. The gold spheres were obtained from Joris Koek and synthesized according to the procedure described by Guo et al.<sup>40</sup> The silica coated gold rods and super particles were obtained from Harith Guanarayanan.

### Particle characterization and sample preparation

With a Scanning Electron Microscope (SEM, FEI Verios 460) the obtained particles were analyzed. The particles were analyzed using a python script (Appendix 1). With the script, the diameter and the aspect ratio of the particles could be estimated. To separate particles in the image a watershed function was used. However, sometimes multiple particles were still analyzed as a single particle. As the shape of the spherical particles did not deviate much from a circle, boundary conditions were applied to the aspect ratio to separate the single particles from the aggregated particles. With this method particle size distribution could be obtained for the spherical gold and thermometer particles. The particle size for the batch of smaller thermometer particles was  $14 \pm 6$  nm (Fig. 5a), while it was  $30 \pm 4$  nm for the batch of bigger particles (Fig. 5b).

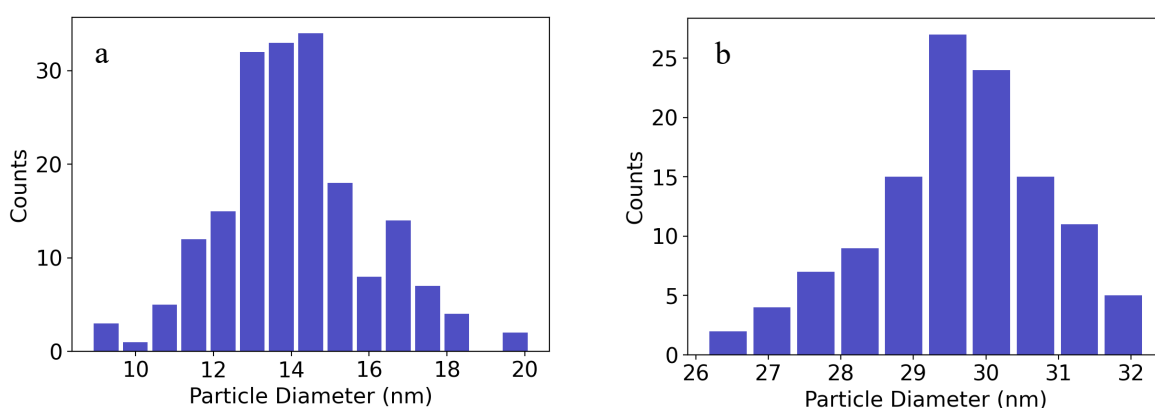


Figure 5: Particle size distribution for the  $\text{NaYF}_4:\text{Er}^{3+}, \text{Yb}^{3+}$  particles of the a) smaller batch ( $\pm 14$  nm) b) bigger batch ( $\pm 30$  nm).

The spherical gold particles, although the number of measured particles was low, have a particle size of approximately 55 nm (Fig. 6a). For the gold rods it was not possible to set boundary conditions for the aspect ratio, as this could vary per particle. Therefore, only completely separated particles were analyzed. Because the resonance of gold rods is mostly determined by their aspect ratio this is plotted in figure 6b. The measured gold rods had a size of approximately 60 x 30 nm with a silica coating of 20 nm thick.

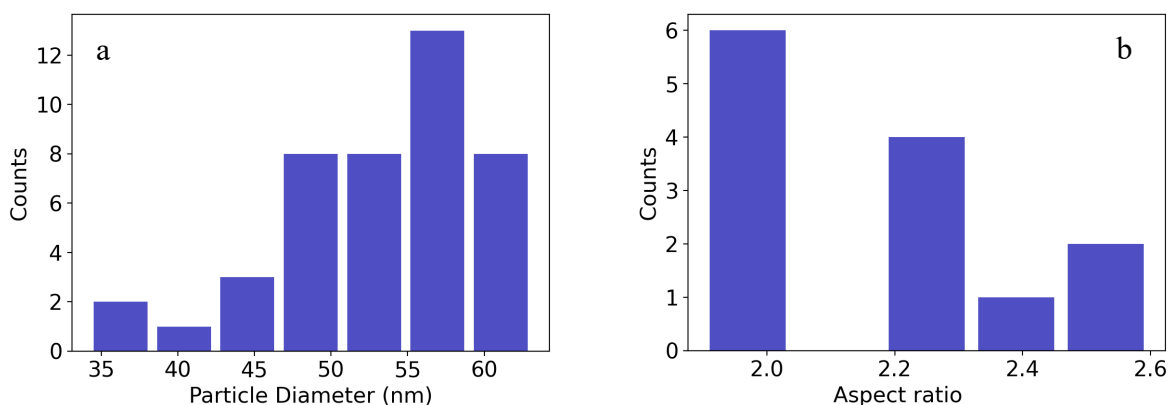


Figure 6: a) Particle size distribution of spherical gold nanoparticles. b) aspect ratio distribution of gold nanorods.

Using the described particles, samples were prepared on glass coverslips and indium tin oxide (ITO) covered glass coverslips for photoluminescence and on sillicium for cathodoluminescence measurements. For photoluminescence first a monolayer of the thermometer particles, with a diameter of  $\pm 14$  nm (10x diluted, droplet of 100  $\mu\text{L}$ ), was spincoated at a rate of 3000 rpm for 70 seconds. Then the gold spheres (10x diluted, droplet of 50  $\mu\text{L}$ ) were spincoated on the glass sample and the rods (50x diluted, droplet of 50  $\mu\text{L}$ ) were spincoated on the ITO sample at a rate of 2000 and 3000 rpm for 70 seconds respectively (Fig. 7a,b). For the cathodoluminescence samples the thermometer particles were replaced by the bigger particles ( $\pm 30$  nm) to increase the signal of the measurements.<sup>37</sup> The samples were prepared by spincoating the thermometer particles (5x diluted, droplet 100  $\mu\text{L}$ ) at a rate of 3000 rpm for 70 seconds, followed by spincoating of the gold rods (50x diluted, droplet 50  $\mu\text{L}$ ) at a rate of 3000 rpm for 70 seconds (Fig. 7c).

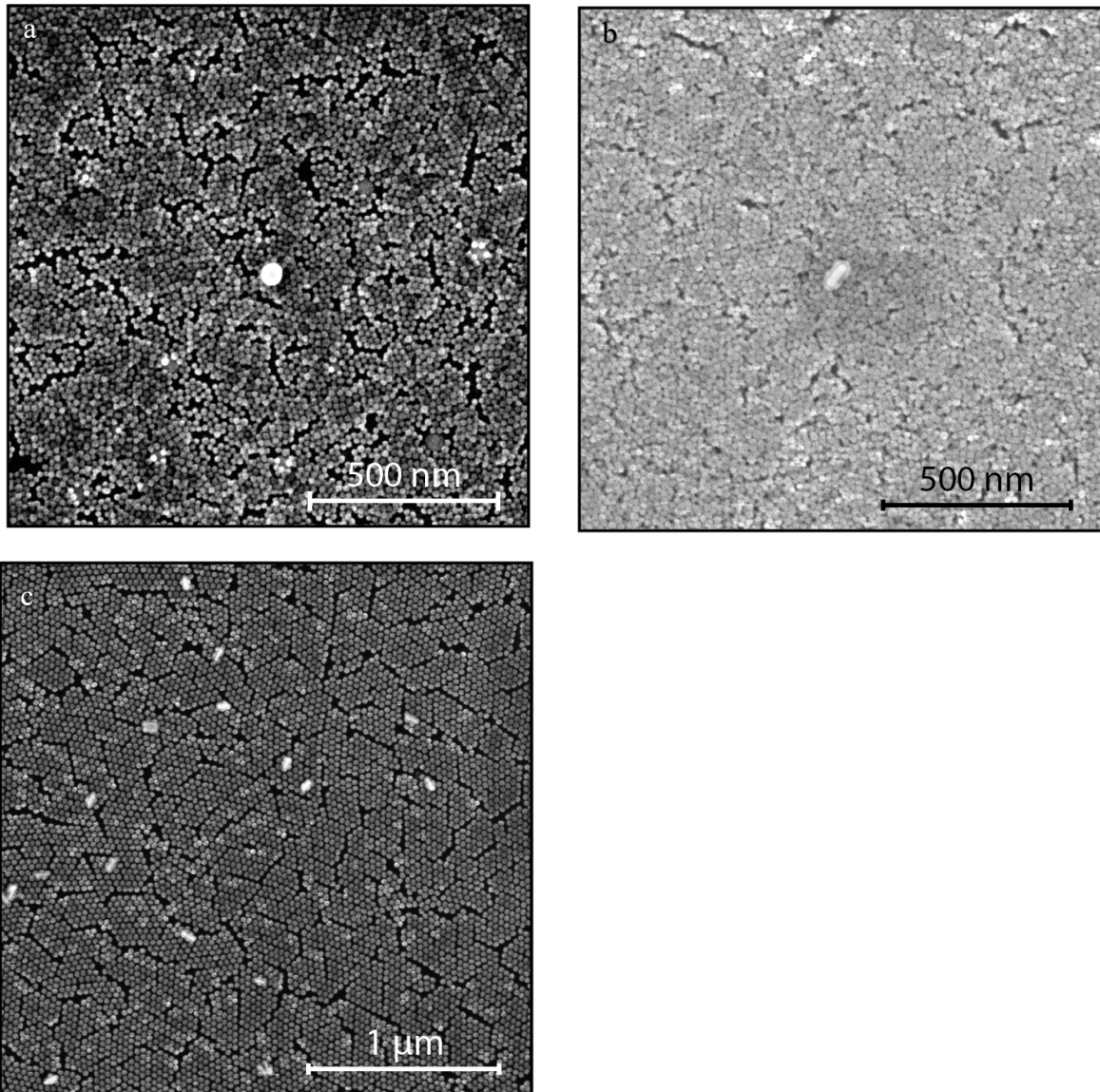


Figure 7: SEM image of sample prepared on a) glass substrate with a monolayer of the thermometer particles ( $\pm 14$  nm) and single gold spheres ( $\pm 58$  nm). b) glass with ITO substrate with a monolayer of the thermometer particles ( $\pm 14$  nm) and single gold nanorod ( $\pm 30 \times 60$  nm). c) silicon substrate with a monolayer of the thermometer particles ( $\pm 30$  nm) and single gold nanorod ( $\pm 30 \times 60$  nm).

### Photoluminescence experiments

Photoluminescence measurements were performed on a home-built microscopy setup (Fig. 8b). In this setup the sample was placed on a Nikon Ti-U inverted microscope. Scattering was measured using a white light source, for which high angle light ( $> 14^\circ$ ) was blocked by a pinhole (Fig. 8a,b). This high angle light was directed to the sample by a 50/50 non-polarizing beam splitter and guided into an oil-immersion objective (Nikon CFI Plan Apochromat Lambda 100x, NA 1.45). The low angles of the light, mainly consisting of reflected light (Fig. 8a), were then blocked in the Fourier plane using a 3D printed beam blocker. After positioning the beam blocker, the Fourier lens was removed to collect the scattered light on a spectrograph (Andor Kymera 193i), equipped with an electron-multiplying charge-coupled device director (EMCCD, Andor iXon Ultra 888). A slit positioned in front of the EMCCD could be closed to decrease the collected light in the x-direction. By switching the grating in the EMCCD to first order a

spectrum could then be collected. For the heating experiments two excitation light sources were aligned on the same spot entering the microscope using a series of mirrors and a 90/10 beam splitter. The 980 nm laser was placed in the reflection of the beam splitter and the heating laser (637/730 nm laser) was placed in transmission to maximize the heating output. After entering the microscope, the light was directed to the sample with a beam splitter placed above the white light source beam splitter. The two beamsplitters were used subsequently as the signal was sufficient after halving. After position the lasers the slit was closed, and the grating turned to first order to collect the emission spectra on the spectrograph.

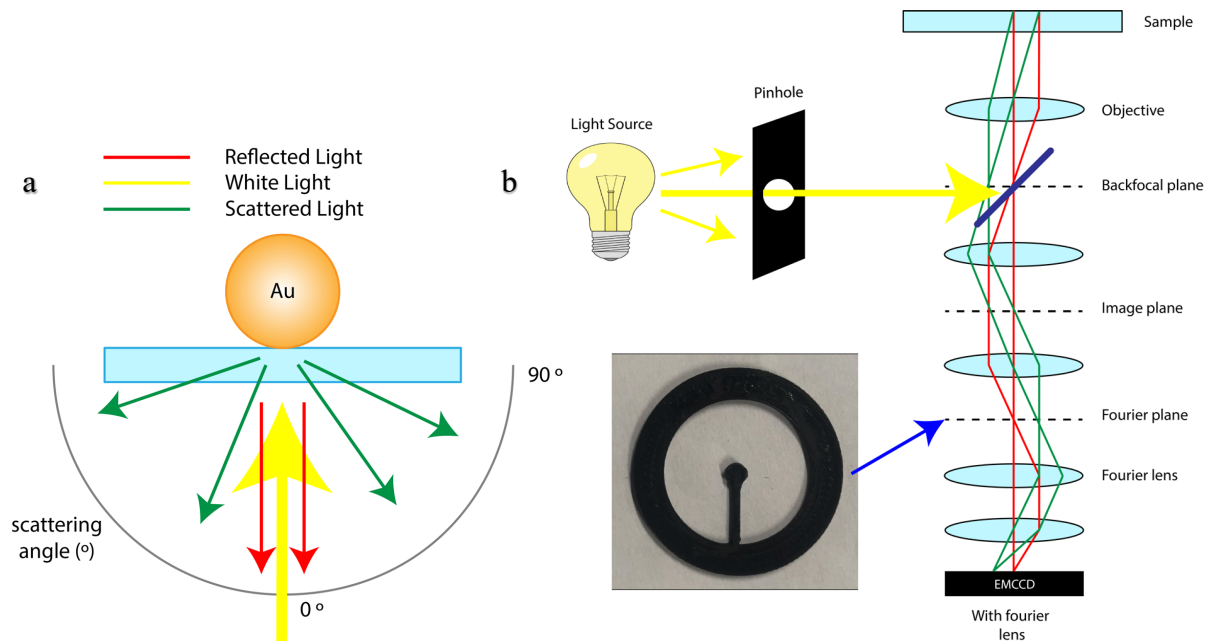


Figure 8: a) Schematic representation of scattering on gold nanoparticles. Small angles contain most of the reflected light and are therefore blocked. b) Schematic representation of the microscopy setup used for photoluminescence measurements. High angle light is blocked by a pinhole and later in the Fourier plane the lower angles containing reflected light are blocked to maximize the scattering signal.

### Cathodoluminescence experiments

Cathodoluminescence measurements were performed in a SEM (Thermo Fisher Quanta 650) equipped with a Schottky field emission gun (FEG). During the experiments the sample was placed in the vacuum chamber of the SEM and illuminated with a continuous beam of electrons, with an acceleration voltage of 5 keV. By mounting a parabolic mirror above the sample, the CL signal was redirected out of the chamber into the Delmic Sparc Spectral system, where the collected light was focused onto a Newton CCD camera (oxford instruments). Using the emission pattern on the CCD camera the mirror was aligned as such that its focal point corresponded with that of the electron beam. After alignment of the mirror the CL emission was redirected to a fiber-coupled (550 $\mu$ m diameter core multimode fiber) spectrometer (Acton SP-2300i, Princeton Instruments) with a flip mirror along the optical path. The ODEMIS software was used to raster-scan over a region of interest with the electron beam and both the secondary electrons and a spectrum were simultaneously collected. During the experiments a 300 l/mm grating with a blaze of 500 nm, spot size of 3.9, dwell time of 10  $\mu$ s, gain of 4 and readout rate of 0.05 MHz was used. Lastly, the aperture was varied to change the current of the electron beam.

## Results

The goal of this study was to develop a method to induce and tune the temperature of single gold NPs using light excitation, while subsequently monitoring the temperature around these gold NPs using ratiometric nanothermometry. This section starts by discussing the important emission peaks of erbium for ratiometric nanothermometry. Then a method is established for temperature measurements of strong scattering and absorbing gold supraparticles using PL. This method is then used to measure the temperature of a single spherical gold NP and a single gold nanorod, however with an additional step to determine whether the diffraction limited spot contains a single or multiple NPs. Finally, the method is translated to CL for higher spatial resolution measurements.

### Peak assignment

The emission lines used in nanothermometry for UC particles consisting of  $\text{NaYF}_4:\text{Er}^{3+}, \text{Yb}^{3+}$  are due to the  $^4\text{S}_{3/2}$  and  $^2\text{H}_{11/2} \rightarrow ^4\text{I}_{15/2}$  transitions of the erbium, with emission maximum at 550 and 530 nm, respectively (Fig. 9).<sup>16,37</sup> Apart from emission as a result of two-photon UC processes there is also emission due to three-photon UC processes. The population in the  $^2\text{H}_{9/2}$  state and its radiative relaxation with an emission maximum at 560 nm to the first excited state,  $^4\text{I}_{13/2}$ , are dependent on such three-photon UC processes.<sup>37,41</sup> Comparison of our emission spectrum with those reported in literature shows a small deviation in the wavelength of a few nm. This might be the result of a small misalignment between the slit and grating in the EMCCD. However, this small deviation should not cause any issues for calculation of the temperature because the integration range was changed accordingly.

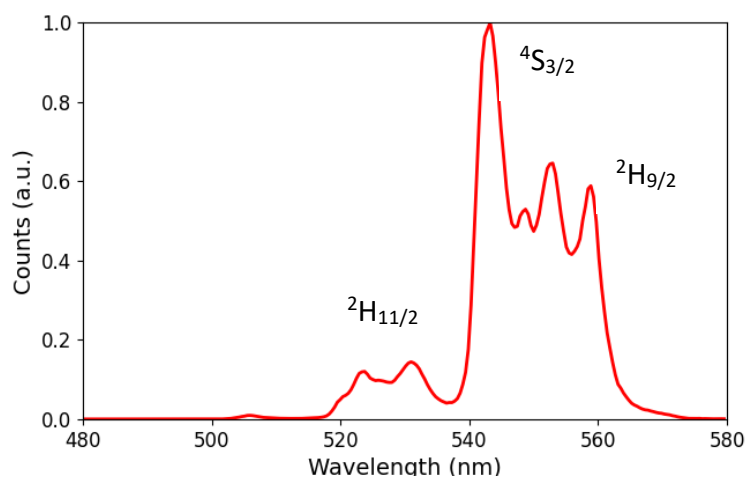


Figure 9: Emission spectrum of erbium, the ratio between the  $^2\text{H}_{11/2}$  and  $^4\text{S}_{3/2}$  emission intensity is used for ratiometric nanothermometry. The  $^2\text{H}_{9/2}$  emission is 980 nm excitation power dependent and should be minimized as it can introduce an error in temperature calculations.

### Photoluminescence

#### Supraparticles

To develop a method for temperature measurements using PL a first experiment was done using gold supraparticles. We chose those clusters of gold particles because they are expected to cause significant heating upon illumination at their resonance and show strong scattering of light, since both the absorption and the scattering scale with volume. Due to this strong scattering, the gold supraparticles could be easily located on the cover slip by collecting a

scattering intensity map. Figure 10 shows a scattering intensity plot of the deposited supraparticles with the bright regions corresponding to the gold.

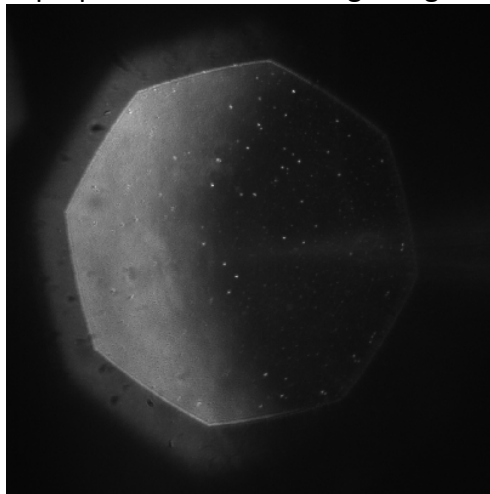


Figure 10: Scattering intensity map for sample with gold supraparticles. The bright scattering plots show regions with gold particles.

After localizing a scattering region, it was positioned at the middle of the detector and a 980 nm laser, for UC excitation of the Erbium, and a 637 nm laser, for the heating of the gold particles, were focused on the gold region. The 637 nm laser was chosen because it was expected to overlap with the resonance of the supraparticles and therefore result in heating of the particles.

At first the gold particles were solemnly illuminated with the 980 nm laser and the luminescence intensity ratio (LIR) between the  ${}^2\text{H}_{11/2}$  and  ${}^4\text{S}_{3/2}$  emission was calculated for each height in the slit. Although, no heating was expected due to 980 nm illumination the peak ratio was not constant. This could be the result of photonic effects.

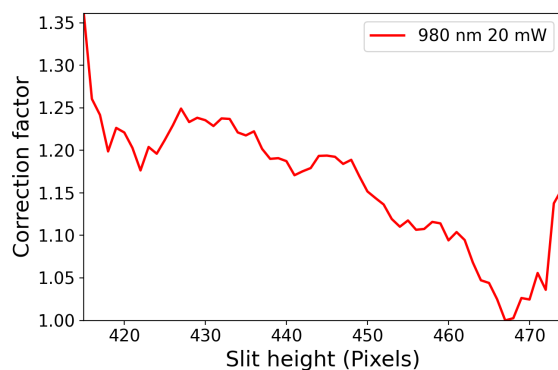


Figure 11: The calculated correction factor for the LIR at all positions in the slit. This factor is used to correct the data collected during temperature measurements.

We assume room temperature over the whole sample upon 980 nm illumination, the data was therefore corrected at each position in the slit with a correction factor. This factor was calculated for each position according to (Fig. 11):

$$\text{correction factor} = \frac{LIR_i}{LIR_{min}} \quad [14]$$

We assume the shape of the correction factor is only dependent on the 980 nm laser and the measurement region. Since the 980 nm laser power was constant, the correction factor could

be used for all measurements with subsequent illumination by the 637 nm laser at the same position. Therefore, the LIR, measured upon illumination with the 637 nm laser, was corrected by dividing it with the correction factor for each respective position. Figure 12a shows the LIR for positions in the slit close to the gold particle at varying heating power: 20 mW, 50 mW and 120 mW. The LIR has a maximum at pixel 445 for all powers and diminishes upon moving farther away from the gold particles. The LIR is higher at higher excitation powers of the 637 nm heating laser. To check if this change was the result of a temperature effect, the normalized spectra collected at the maxima of the different heating powers are compared in figure 12b. Upon illumination with the 637 nm laser the peaks at 530 nm increased in relative intensity and the peaks at 555 and 560 nm first decreased in intensity and eventually increased at higher powers. The intense peak at 560 nm belongs to the  ${}^2\text{H}_{9/2} \rightarrow {}^4\text{I}_{13/2}$  transition and can partially overlap with the emission from the  ${}^4\text{S}_{3/2}$ . This overlap can result in an overestimation of the  ${}^4\text{S}_{3/2}$  emission and thus in an underestimation of the temperature (Appendix 2).<sup>41</sup> The origin of the changes in the intensity of the peak are unknown but could be the result of a temperature effect or an additional transition due to the 637 nm illumination. The intense  ${}^2\text{H}_{9/2}$  emission upon illumination with the 980 nm laser, was most likely the result of a too high excitation power resulting in relatively stronger three-photon UC to the  ${}^2\text{H}_{9/2}$  state. Furthermore, because the effect of temperature and increased  ${}^2\text{H}_{9/2}$  emission is opposite, with regard to the change in the relative  ${}^2\text{H}_{11/2}$  emission, the increased  ${}^2\text{H}_{11/2}$  emission, which was proportional to the 637 nm excitation power, was assigned to an increase in the temperature. However, the overlapping  ${}^2\text{H}_{9/2}$  and  ${}^4\text{S}_{3/2}$  emission can cause an error in the temperature determination. This error is related to the  ${}^2\text{H}_{9/2}$  emission intensity and therefore a strong underestimation of the temperature was expected, especially for excitation with the 637 nm at a power of 120 mW.

The observed temperature change can be the result of heat diffusion from the heated gold particle or by direct heating of the thermometer particles. To determine if erbium can be excited upon illumination with the 637 nm laser, the total intensity for each position at the different powers was plotted in figure 12c. The total intensity increased significantly upon 637 nm illumination, which shows that erbium can be excited and potentially heated by the laser. As it was shown that the change in LIR is due to a temperature effect the temperature was estimated using the Boltzmann equation (Eq. 13),  $\Delta E = 714 \text{ cm}^{-1}$  from literature<sup>19</sup> and a value for the LIR at room temperature based on the tail of the LIR (Fig. 12a) at 20 mW 637 nm illumination. With the estimated temperature and by converting the slit height from pixels to nm (1 pixel = 130 nm) the temperature of the thermometer layer could be plotted as a function of the distance to the gold supraparticles (Fig. 12d). At 120 mW 637 nm excitation a maximum temperature of 60 °C was observed that diminished over 3  $\mu\text{m}$ . However, at 3  $\mu\text{m}$  from the gold, where heating by the gold is minimal, the temperature stabilized above room temperature. Therefore, the thermometer particles could potentially be heated directly by the 637 nm laser, which is in line with the increased total emission intensity at higher excitation powers.



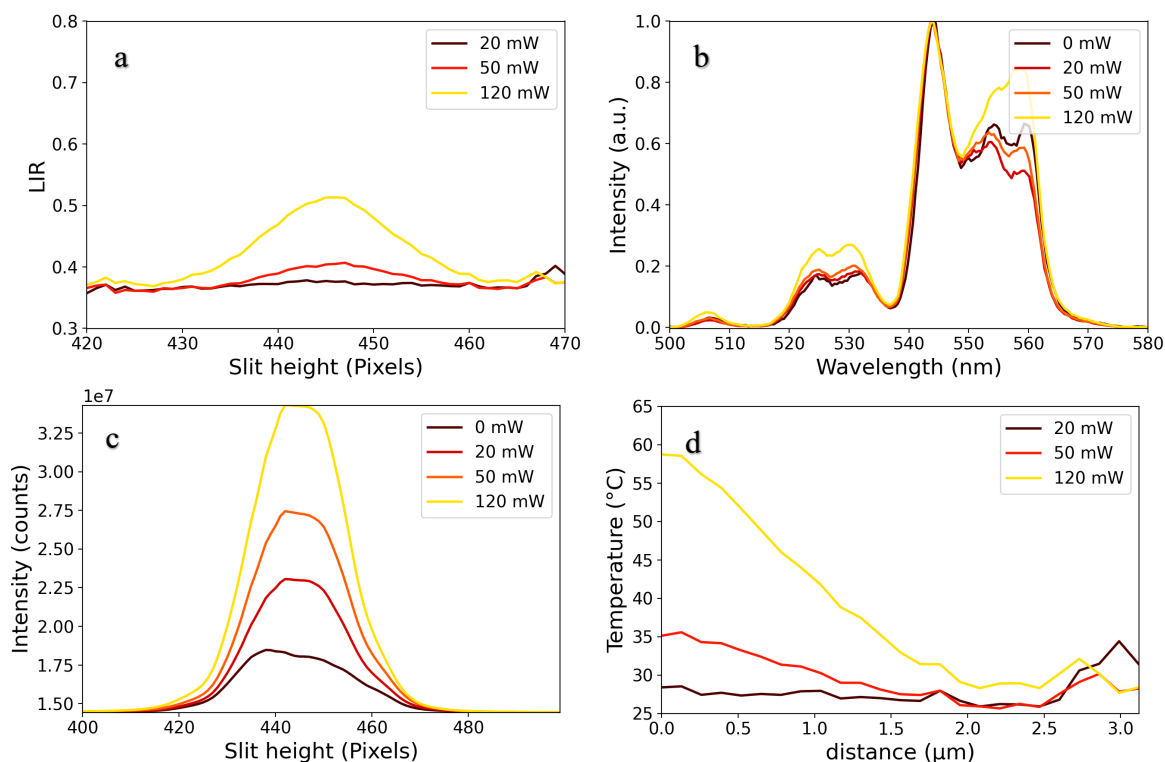


Figure 12: a) LIR for pixels close to the gold particle upon illumination with 20 mW 980 nm and 20, 50 or 120 mW 637 nm laser. b) Emission spectra of erbium collected at the peak of the LIR (pixel 445) for the different 637 nm excitation powers. c) The total intensity of the erbium emission for different illumination powers shows that erbium can be excited by the 637 nm heating laser. d) Temperature profile calculated via the Boltzmann equation using the peak ratio between -3 and -2  $\mu\text{m}$  as room temperature and  $\Delta E = 714 \text{ cm}^{-1}$ .

## Gold spheres

Next step, we can try to apply the method used for supraparticles to induce more localized heating using single spherical gold NPs. We start with spherical NPs with a size of approximately 55 nm and a calculated scattering cross section maximum at 559 nm (Fig. 13a). The same method could be used for temperature measurements on the spherical gold NPs as for the gold supraparticles. However, an additional step was required to determine if scattering occurred on a single gold NP or on multiple NPs close together. Because spherical gold NPs were used with a size much smaller than the diffraction limit, multiple NPs within a diffraction limited spot cannot be distinguished in a dark-field image. The peak wavelength in a scattering spectrum redshifts when multiple particles are close together due to coupling of their dipoles.<sup>30</sup> This possible redshift was therefore used to estimate if scattering occurred on a single NP or on multiple NPs. Scattering spectra were collected for regions with scattering and compared to the calculated scattering spectrum of the spherical gold particles. When the two spectra matched it could be assumed that the scattering occurred on a single NP. It should however be noted that if two NPs are sufficiently far apart, that there is no dipole coupling, the scattering spectrum will look like that of a single NP, while the heating of both gold NPs due to a relatively wide laser spot would still be possible. To minimize the chance of looking at multiple particles in a diffraction limited spot a scattering region was chosen with a relatively low scattering intensity as the presence of multiple particles would result in an increased total scattering intensity.

Figure 13a shows the collected spectra at positions close to the gold NP(s) upon illumination with a white light source. A broad background peak was observed in the spectra, which might

be a result of scattering on the dielectric thermometer particles and the substrate with an approximately flat scattering cross section for all wavelengths. Scattering from these dielectric particles is therefore directly proportional to the spectrum of the used light source. The shape of the background was determined by collecting spectra at a position without gold and is plotted as a reference in figure 13a. Comparing the spectrum and the shape of the white light source, a distinct feature is visible around 550 nm, which could correspond to the presence of a single gold NP. The diameter of the gold NPs ranges from 40 – 60 nm with calculated scattering maxima between 548 and 565 nm (fig spheres and particle distribution). Furthermore, when two particles are close, the maxima of their scattering spectra redshifts. The scattering feature observed in figure 13a has a maximum at 550 nm, corresponding to a gold particle with a diameter of 40 nm. Because 40 nm is at the lower bounds of the particle distribution a redshift due to dipole coupling is unlikely. The spectrum was thus assigned to that of a single gold sphere with a diameter of 40 nm.

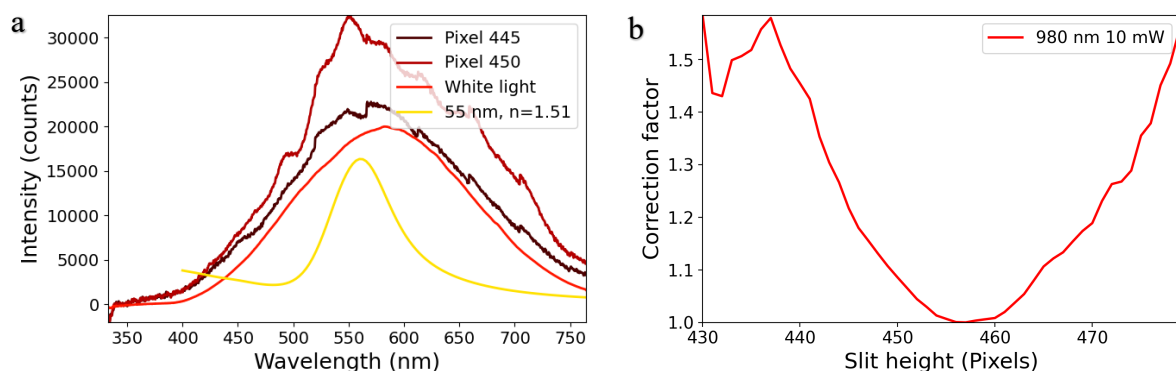


Figure 13: a) Collected scattering for spherical gold nanoparticle collected at pixel 445, compared to the calculated scattering spectrum using Maxwells equations for a sphere of 55 nm with  $n_s=1.51$ . The big background peak matches with the shape of the white light source, which can be visible due to scattering of particles without a resonance and thus with a flat scattering cross section. b) Correction factor for single spherical gold particle obtained by illumination with 10 mW 980 nm laser.

Just as for the supraparticles, heating of the gold spheres was done using a 637 nm laser (5, 15 and 25 mW), because this wavelength matches better with the resonance compared to the 730 nm laser. First a correction factor was calculated for each position (Fig. 13b). Next, the LIR was calculated and corrected by the correction factor (Fig 14a). Figure 14a shows that the maximum of the LIR is positioned at pixel 445, this slightly deviates from the position obtained from scattering. The sample could thus have slightly moved, or the alignment could have changed resulting in this deviation. Increasing the power of the 637 nm laser resulted in an increase in the LIR at all pixels. To determine whether this was a temperature effect the emission spectra at pixel 445 are plotted for all heating powers in figure 14b. Similar changes in the spectra were observed upon illumination with the 637 nm laser compared to the supraparticles. The relative  ${}^2\text{H}_{11/2}$  peak intensity increased, and the  ${}^2\text{H}_{9/2}$  peak intensity first decreased and then increased at higher excitation powers. The precise effect causing this change is still unknown. However, the intensity of  ${}^2\text{H}_{9/2}$  emission was significantly reduced by lowering the 980 nm laser power from 20 mW to 10 mW. Therefore, the error in the temperature was expected to be much smaller compared to the supraparticle measurement.

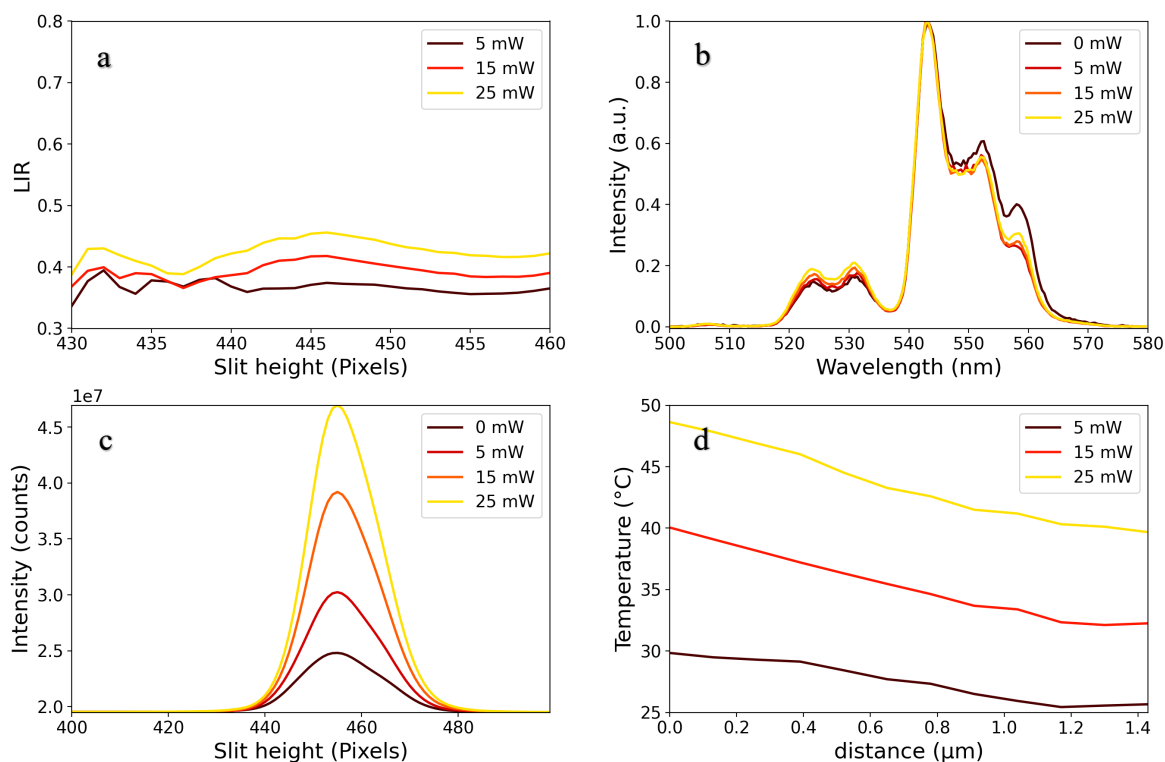


Figure 14: a) LIR versus collection pixel upon illumination with 10 mw 980 nm and 5, 15 or 25 mW 637 nm lasers. b) Emission spectra of erbium collected at the peak of the LIR (pixel 445) for the different 637 nm excitation powers. c) The total intensity is similar to gold supra particles confirming that erbium can be excited by the 637 nm heating laser. d) Temperature profile calculated via similar method as for supraparticles, the different temperatures at 1.4  $\mu\text{m}$  show that the thermometer particles are directly heated by the 637 nm laser.

Again, the total emission intensity increased upon illumination with the 637 nm laser indicating excitation of the erbium and possible direct heating of the thermometer particles (Fig. 14c). The LIR was converted to temperature and the pixels converted to a distance with respect to the gold NP, located at pixel 445 (Fig. 14d). Figure 14d shows that the maximum temperature of the gold was 48  $^{\circ}\text{C}$  at a 637 nm excitation power of 25 mw and diminishes over 1.5  $\mu\text{m}$ . Even more clear, compared to the supraparticle measurement the temperature stabilized above room temperature. This temperature was related to the excitation power. This stronger effect for the gold spheres can be the result of the position of the temperature tail with regard to the total intensity of the beam at that position. The tail for the spheres corresponds to a position in the slit at pixel 455 at which the total intensity (Fig. 14c) is still high, compared to the total intensity for the supraparticles at pixel 465. Heating of the thermometer particles was thus dependent on the 637 nm excitation power, even at positions sufficiently far from the gold that heating by the gold was minimal. This confirms that the thermometer particles were directly heated by the 637 nm laser.

### Gold rods

Now that we were able to measure a temperature profile induced by a single gold NP, we want to increase the plasmonic heating of the gold. Therefore, we use gold nanorods with dimensions of approximately 30x60 nm and a higher absorption cross section at its resonance compared to the spherical NPs. We also switched from a glass substrate to a glass substrate covered with a thin layer of ITO, so we could measure our samples with both PL and SEM. Therefore, the refractive index of the effective medium changed slightly to approximately 1.65. Calculating the cross sections for these conditions gives a scattering peak at 701 nm (Fig

15a). This matches well with the wavelength of the 730 nm laser and heating could therefore be increased significantly compared to the previous experiments.

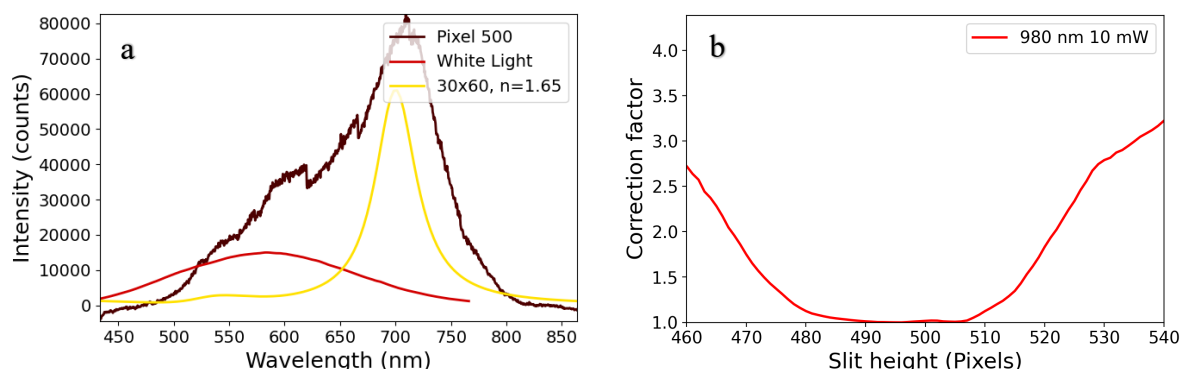


Figure 15: a) Collected scattering for gold nanorod collected at pixel 500, compared to the calculated scattering spectrum using Maxwells equations for a gold rod of 30 x 60 nm with  $n_s=1.65$ , the peaks match suggesting scattering belongs to a single gold nanorod. The shape of the white light source is vaguely visible due to the much stronger scattering of the rod compared to a sphere. b) Correction factor for single gold nanorod obtained by illumination with 10 mW 980 nm laser.

First, scattering spectra were collected for a region with moderate scattering intensity. Figure 15a shows the spectrum collected at the position of the gold nanorod and the reference spectrum of the white light source. A strong scattering peak is visible at approximately 710 nm this coincides with the calculated scattering peak at position 701 nm We therefore assumed that we were measuring a single gold nanorod. From illumination by the 980 nm laser the correction factor was determined (Fig. 15b) and then applied to the LIR of the measurements with subsequent illumination by the 730 nm laser (Fig. 16a).

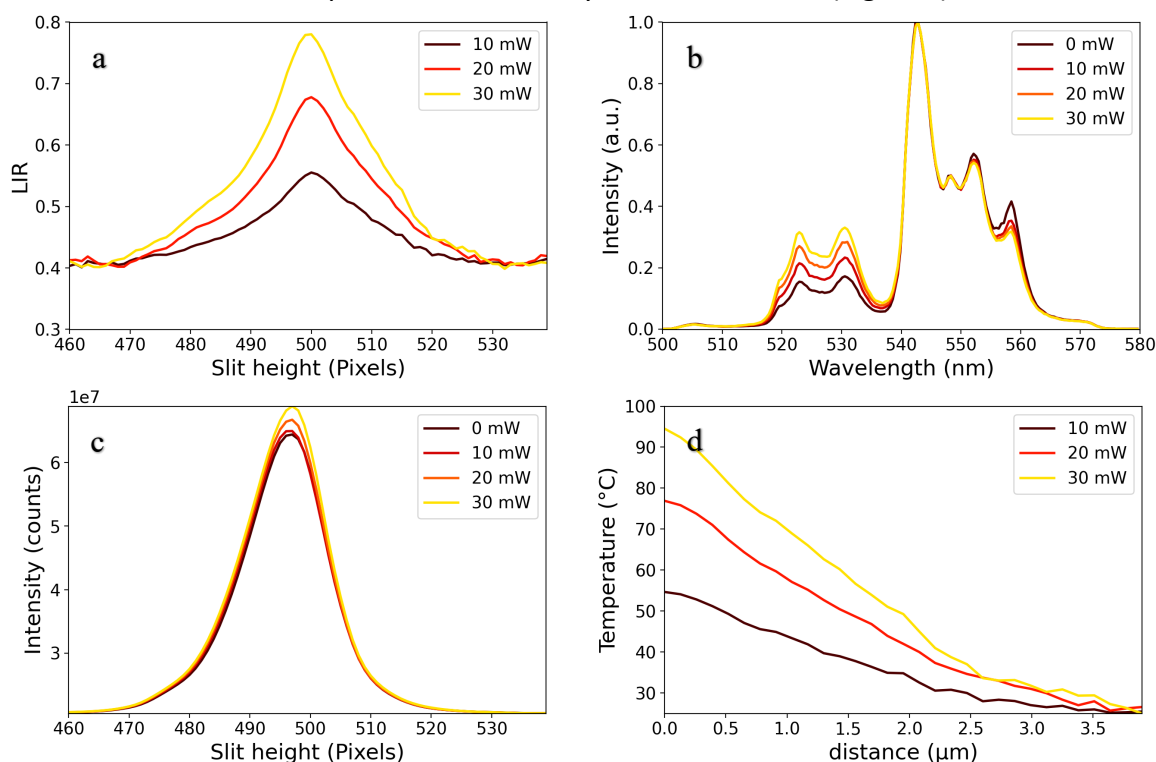


Figure 16: a) LIR versus collection pixel under illumination of 980 nm (10 mw) and 730 nm laser (10, 20 and 30 mw). b) Luminescence emission spectra of Erbium collected at pixel 500 under illumination of 980 nm (10 mw) and 730 nm (0, 10, 20 and 30 mw) laser. c) Total emission intensity is similar for different 730 nm excitation powers showing that the erbium cannot be directly excited upon 730 nm illumination. d) Temperature of thermometer particles versus the distance to the gold nanorod. The temperature diminishes to room temperature in approximately 4  $\mu\text{m}$  so no direct heating of the thermometer particles due to 730 nm illumination.

This resulted in a LIR profile featuring a sharp peak at pixel 500, which coincides with the position of the single gold nanorod scattering spectrum. This peak looks symmetric on both sides and increased proportional to the excitation power. The change in the LIR upon excitation with the 730 nm laser was much bigger than the change due to illumination of the spherical gold and gold supraparticles with the 637 nm laser (Fig. 12a and 14a). To determine whether this significant increase was due to stronger heating of the gold particle, the normalized emission spectra collected at pixel 500 are plotted for the different 730 nm excitation powers in figure 16b. These spectra show that the  $^2\text{H}_{11/2}$  emission intensity increased proportional to the excitation power of the 730 nm laser. Furthermore, the  $^2\text{H}_{9/2}$  emission intensity decreased significantly upon excitation with the 730 nm laser and decreased slightly further at higher excitation powers. This observation deviates from that with 637 nm excitation as higher excitation powers there resulted in a more intense  $^2\text{H}_{9/2}$  peak. To compare the different excitation lasers the total intensity upon 730 nm illumination is plotted in figure 16c. This total intensity plot shows that the intensity did not change much upon subsequent illumination with the 730 nm laser. The decrease in the  $^2\text{H}_{9/2}$  emission intensity could therefore be a temperature effect, while the increasing  $^2\text{H}_{9/2}$  emission for higher excitation power of the 637 nm could be the result of increased erbium excitation. Because the intensity of the  $^2\text{H}_{9/2}$  emission is relatively low for the gold nanorod experiment, so is the expected error in the temperature. The calculated temperature versus the distance to the gold nanorod is plotted in figure 16d. The temperature increase for the different powers seems to be linear, which would be expected as the absorbed energy by the gold particle is proportional to the illumination of the particle. A maximum temperature of 95 °C was measured at 30 mW 730 nm excitation and the temperature diminished over approximately 3.5  $\mu\text{m}$ . With 730 nm excitation the temperature did seem to return to room temperature sufficiently far away from the gold. This indicates that direct heating of the thermometer particles was absent or only limited upon 730 nm excitation.

### Cathodoluminescence

With PL we were able to induce, tune and monitor light-to-heat conversion at the micrometer scale. However, PL measurements are diffraction limited and thus limited in spatial resolution. Therefore, a different technique is needed to study light-to-heat driven catalytic reactions at the nanoscale. To get information at the nanoscale we need CL, which beats the diffraction limit of light as the signal is picked up using a scanning electron beam. For CL experiments we used similar samples compared to PL. However, we replaced the ITO substrate by a silicium substrate and used the bigger thermometer particles, with a diameter of 30 nm, to increase the signal obtained with CL.<sup>37</sup> As plasmonic heating source we used the same gold nanorods as for PL because they induced strong localized heating in our prior experiments. Heating of the gold nanorods as well as CL collection of the thermometer particles were both done through excitation with an electron beam. Consequently, only temperature measurements on gold versus off gold and measurements at different electron beam currents could be studied. Since a temperature profile around the gold could be caused by less heating of the gold by the electron beam and/or less heat diffusion to thermometer particles upon focusing the electron beam farther away from the gold.

To determine the optimal operating voltage for the CL measurements, monte carlo simulation of electron trajectory in solids (Casino) was used to estimate the proportion of the CL signal originating from a certain depth in the sample for different acceleration voltages (Appendix

3). Upon increasing the acceleration voltage from 1 keV to 5 keV the CL signal originating from the thermometer particles, the upper 40 nm of the sample, decreased from approximately 100% to 13% of the total emission. A further increase to 10 keV resulted in only 5% of the CL originating from the region of interest. It was therefore important to minimize the operating voltage to maximize the signal-to-noise ratio. However, the spatial resolution of the SEM decreased drastically at lower voltages. Therefore, experiments were performed using the lowest operating voltage with sufficient spatial resolution, 5 keV.

Extracting temperature information from the CL signal was done using, the ratio between the  $^2H_{11/2}$  and  $^4S_{3/2}$  emission to the ground state, the same method as used for photoluminescence. A different method, proposed in the work of Aiello et al<sup>21</sup>, uses the ratio between the  $^4F_{9/2}$  and the  $^4S_{3/2}$  emission to the ground state. This method was validated for the determination of the temperature around a plasmonic gold particle. However, the two used states in this method are not thermally coupled and belong to absorption processes of a different order, which results in a power dependent peak ratio and therefore a new calibration would be needed for each measurement at different conditions.<sup>42</sup>

First, the effect of the electron beam on the thermometer particles was investigated by measuring CL spectra at regions without gold for three different electron currents: 130 pA, 293 pA and 528 pA. At each of these currents three different regions were measured. By taking the sum of all measurements at a certain current, the signal-to-noise ratio was sufficient to distinguish the peaks. Figure 17 shows the summed spectra for the different electron currents. The spectra all look very similar except for the change in the shape of the 550 nm peak at higher electron beam currents. This could be the result of an increased emission from the  $^2H_{9/2}$  level as was observed in photoluminescence, however the CL spectra were too noisy to draw any definitive conclusions. The peaks at 530 nm and 660 nm for the different currents seem to overlap, this could suggest that according to both methods, the LIR, and thus the temperature of the thermometer particles, was independent of the current.

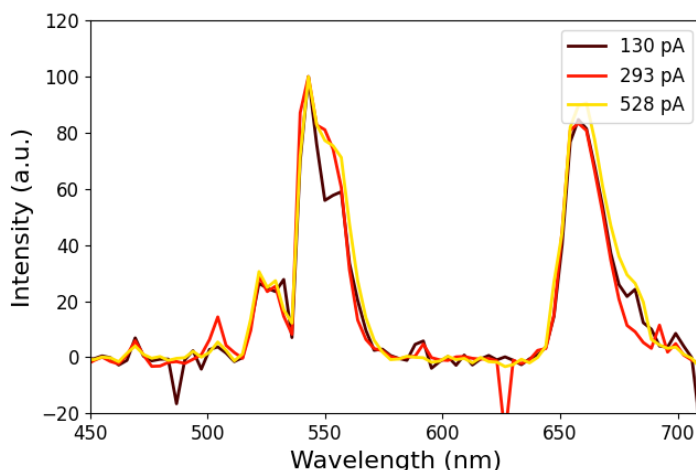


Figure 17: Cathodoluminescence spectra of monolayer  $NaYF_4:Er^{3+}, Yb^{3+}$  thermometer particles at different electron beam currents: 130, 293 and 528 pA. Considering the peak ratio's the thermometer particles are not heated under the electron beam.

Since no heating of the thermometer particles by the electron beam was observed, it was now possible to focus the electron beam at a gold particle and study the erbium emission at and around the gold particles for different electron beam currents. During all measurements

next to the collection of emission spectra a secondary electron image was collected of the scanned area, which was used to estimate the position of the gold particle during the measurements (Fig. 18a). The emission spectra were corrected by subtracting a dark spectrum, averaging each pixel with its eight neighbors, and using a polynomial fit to remove the background. Then the LIR was determined for each pixel and plotted in a heatmap using the ratio between the  ${}^2H_{11/2}$  and the  ${}^4S_{3/2}$  (Fig. 18b). The LIR seemed to be the highest on top of the gold and decreased moving away from the gold. Furthermore, the position of the gold particle seemed to have slightly changed during the measurement.

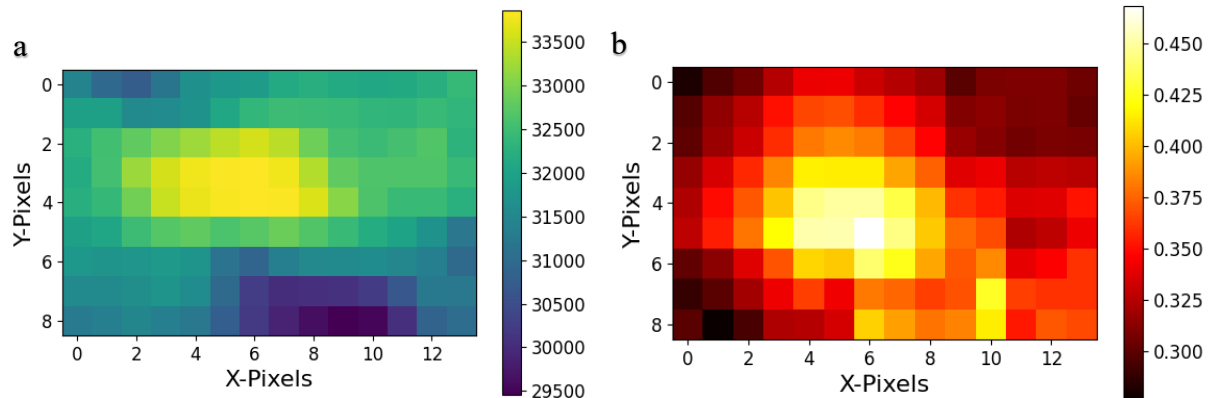


Figure 18: a) Back-scattered electron plot of single gold rod. The brighter pixels show the position of the gold. b) Heatmap for the  ${}^2H_{11/2}$  /  ${}^4S_{3/2}$  luminescence intensity peak ratio, the peak ratio seems higher at the position of the gold.

To compare the different LIR on and off the gold and determine if this difference could be a temperature effect, the spectra of the pixels corresponding to either on or off the gold were summed.

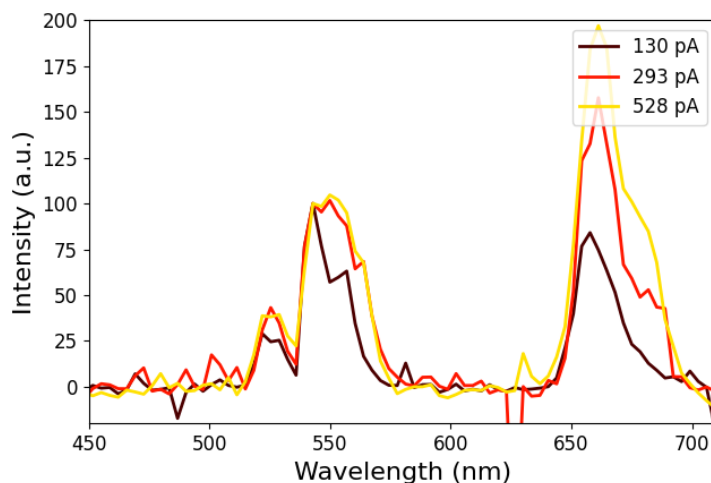


Figure 19: Cathodoluminescence spectra collected around a gold nanorod at different electron beam currents: 130, 293 and 528 pA.

Figure 19 shows the summed spectra for pixels not belonging to a gold particle. Although, the spectra were, especially at higher currents, very noisy a few features could be observed. Upon increasing the electron beam current the peak at 670 nm increased in relative intensity. According to Aiello et al<sup>21</sup> this could be the result of an increase in the temperature of the thermometer particles, which would then be the result of plasmonic heating by the gold as no such change was observed for the regions without gold (Fig. 17). Furthermore, a shoulder was observed at the right-hand side of the 550 and 650 nm peaks for the measurements at 293 and 528 pA. Also, the peaks at 520 – 530 nm have increased in relative intensity. However,

the shape stayed the same for the latter measurements. The changes in the 550 nm peaks could be the result of the same effect observed in the measurement with only thermometer particles. However, the shape seemed to be different, it could therefore also be a plasmonic effect of gold, as gold rods in vacuum ( $n_s=1$ ) have a resonance at 557 nm (for a rod with dimensions of 30x60) (Fig. 20).

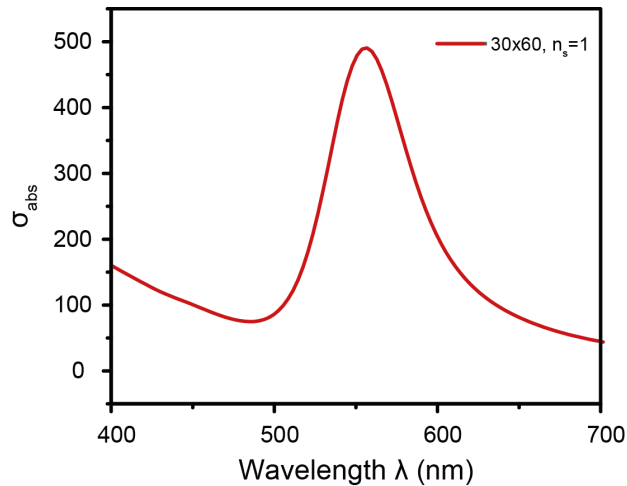


Figure 20: Calculated scattering spectrum for a gold rod in vacuum ( $n_s=1$ ) with dimensions of 30 x 60 nm.

Looking at the spectra of the on-gold pixels, similar things were observed (Fig. 21). Again, the shape of the 550 and 670 nm peaks changed, and the intensity of the 670 nm peak increased with the electron beam power. The spectrum at the highest current had a significant background and could not be fully corrected by a polynomial fit. Therefore, the spectrum looks significantly different from the others. Similarly, to the spectra for the off-gold pixels, the peak at 670 nm increased with electron beam current. However, this increase looks significantly weaker, while the opposite would be expected if this would be a temperature effect. The ratio between the  $^4F_{9/2}$  and the  $^4S_{3/2}$  transition peaks was therefore affected by the presence of gold and thus not a good indication for the temperature in this system.

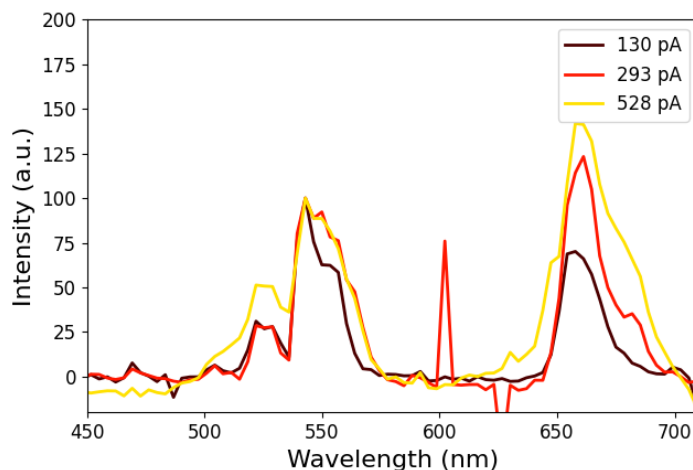


Figure 21: Cathodoluminescence spectra collected at the position of a gold nanorod at different electron beam currents: 130, 293 and 528 pA.

To determine if the  $^2H_{11/2} / ^4S_{3/2}$  LIR is viable for temperature measurements in this system, first the signal-to-noise ratio had to be increased. Therefore, the sum of the different measurements at the same current was used and compared to the measurement with only thermometer particles (Fig. 22). The spectra overlap except for the peaks at 530 and 670 nm.



The peak at 670 nm is less intense on top of the gold compared to the other measurements, confirming that its intensity was affected by the presence of gold. The peak at 530 nm is more intense on top of the gold, while the peaks at 550 nm overlap, therefore it is unlikely that this was an effect of the plasmonic resonance of gold. This could thus be the result of a temperature increase. To confirm whether this was indeed the result of the plasmonic heating of the gold, the intensity, and thus the peak ratio, should increase further upon increasing the electron beam current. However, the signal-to-noise ratio at higher currents is too low to compare and thus no definitive conclusion could be drawn.

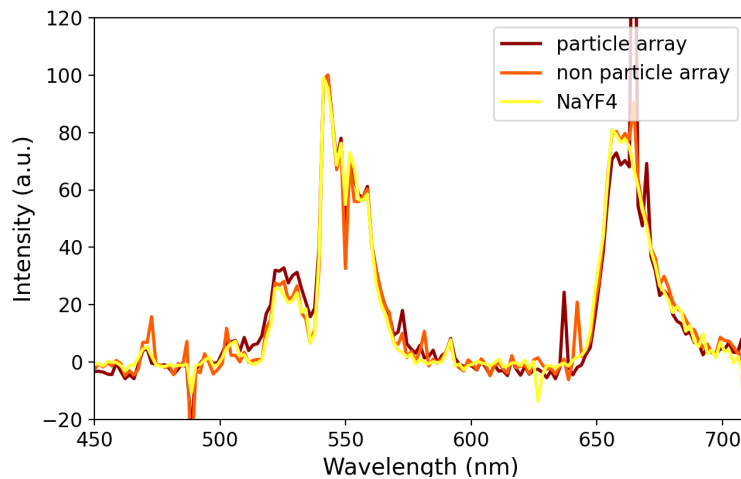


Figure 22: Cathodoluminescence spectra of region with only thermometer particles, around a gold particle and at the position of a gold particle with an electron beam current of 130 pA.

## Conclusion

In this thesis, the plasmonic heating of gold nanoparticles was studied with ratiometric nanothermometry using  $\text{NaYF}_4:\text{Er}^{3+}$  (2%),  $\text{Yb}^{3+}$  (18%) thermometer particles. Luminescence emission was collected using photoluminescence and cathodoluminescence. A procedure was developed for PL to localize and characterize gold nanoparticles, induce and tune their localized heating, and monitor a temperature profile at a micrometer scale resolution. With scattering, gold particles were localized and based on the scattering spectrum an estimation could be made on the presence of a single or multiple gold nanoparticles. Localized heating of the gold particles was induced and could be tuned by matching the plasmon resonance with an excitation laser, 637 or 730 nm, and by varying the excitation power. For 637 nm illumination direct excitation of the erbium was observed, resulting in the undesired direct heating of the thermometer particles. Upon 730 nm excitation no such direct heating was observed, while significant heating of gold nanorods could be induced due to overlap with the plasmon resonance. The temperature profile around the gold nanoparticles was monitored using the temperature-dependent luminescence ratio of the thermally coupled,  $^2\text{H}_{11/2}$  and  $^4\text{S}_{3/2}$ , states in erbium upon illumination with a 980 nm laser. To ensure accurate temperature determination, measurements were corrected for their photonic environment and overlap between emission from the  $^4\text{S}_{3/2}$  and the emission lines, observed at higher 980 nm excitation power, from the  $^2\text{H}_{9/2}$  state was minimized. However, for spatial and temperature information at the nanoscale, PL was not a viable technique due to the diffraction limit of light.

Therefore, CL, which beats this diffraction limitation, was used in combination with SEM. The biggest challenge in CL was the signal-to-noise ratio. Part of the problem was the high

penetration depth of the electrons at 5 keV, which was the voltage needed for sufficient spatial resolution. The signal-to-noise ratio was slightly increased by increasing the size of the thermometer particles and by averaging over multiple spectra. However, the signal was still low, especially for measurements at higher electron beam currents in the proximity of gold. It could be determined that the temperature of the thermometer particles was independent of the electron beam current, which is a requirement for high accuracy temperature measurements. Furthermore, the method proposed for temperature measurements on  $\text{NaYF}_4:\text{Er}^{3+}$ ,  $\text{Yb}^{3+}$  in CL by Aiello et al.<sup>21</sup>, using the luminescence intensity ratio between emission from the  $^4\text{F}_{9/2}$  and the  $^4\text{S}_{3/2}$  state to the ground state, was invalidated for experiments with gold as the ratio was strongly affected by the presence of gold. Furthermore, upon illumination of an area with a gold particle, using an electron beam with a current of 130 pA, the  $^2\text{H}_{11/2}$  emission increased relative to the  $^4\text{S}_{3/2}$  emission, while the rest of the spectra overlapped. This could correspond to a temperature increase, however measurements at higher currents with sufficient signal-to-noise are required to confirm this trend.

The described method for temperature measurements at the micrometer scale using PL, opens up possibilities for localized light-to-heat driven catalysis around a single gold nanoparticle. Furthermore, a first step towards temperature measurements at the nanoscale using CL was taken. Further investigation of this latter method could eventually lead to accurate temperature control at the nanoscale with a wide field of applications.

## Outlook

Although the first steps have been taken towards a method, useful for measuring temperature profiles around a single gold particle, a lot can still be improved for both cathodoluminescence and photoluminescence. Starting off with photoluminescence, in future experiments the power of the 980 nm laser should be further decreased to minimize the effect of overlapping  $^2\text{H}_{9/2}$  and  $^4\text{S}_{3/2}$  emission that can distort temperature measurements. Furthermore, measurements of a sample with only thermometer particles at a low 980 nm excitation power can give additional information on the direct effect of the heating lasers on the thermometer particles. By correlating SEM images to certain positions on the sample in PL more spatial information can be obtained. This can be done by preparing samples on small TEM grids and writing a computer script that correlates scattering intensity images to SEM images. Another interesting experiment in PL would be to do multiple cycles of heating and determine whether heating changes per cycle due to reshaping of the gold particles. Lastly, it would be interesting to design a setup that splits up emission from the erbium into two paths. By using filters to only let either  $^2\text{H}_{11/2}$  or  $^4\text{S}_{3/2}$  emission pass the LIR can be measured in both the x as y direction and therefore a 2D temperature plot can be measured.

In the case of cathodoluminescence the main challenge remains the signal-to-noise ratio. A possibility would be to replace yttrium in  $\text{NaYF}_4$  by the heavier atom lutetium as this could increase the absorption of electrons. Another possibility would be to add extra layers of thermometer particles. This would make temperature measurements less accurate but could enable temperature measurements. Also, it would be interesting to couple in a laser fiber, preferably 730 nm, to enable plasmonic heating of the gold particles with a laser instead of the electron beam.

## References:

- (1) Rostrup-Nielsen, J. R. Fuels and Energy for the Future: The Role of Catalysis. *Catal. Rev. - Sci. Eng.* **2004**, *46* (3–4), 247–270. <https://doi.org/10.1081/CR-200036716>.
- (2) Brongersma, M. L. Introductory Lecture: Nanoplasmonics. *Faraday Discuss.* **2015**, *178* (May), 9–36. <https://doi.org/10.1039/c5fd90020d>.
- (3) Baffou, G.; Quidant, R. Thermo-Plasmonics: Using Metallic Nanostructures as Nano-Sources of Heat. *Laser Photonics Rev.* **2013**, *7* (2), 171–187. <https://doi.org/10.1002/lpor.201200003>.
- (4) Faraday, M. Experimental Relations of Gold (and Other Metals) to Light. *Phil. Trans. R. Soc.* **1857**, *147* (0), 145–181.
- (5) Lalis, A.; Tessier, G.; Plain, J.; Baffou, G. Quantifying the Efficiency of Plasmonic Materials for Near-Field Enhancement and Photothermal Conversion. *J. Phys. Chem. C* **2015**, *119* (45), 25518–25528. <https://doi.org/10.1021/acs.jpcc.5b09294>.
- (6) Baffou, G.; Quidant, R. Nanoplasmonics for Chemistry. *Chem. Soc. Rev.* **2014**, *43* (11), 3898–3907. <https://doi.org/10.1039/c3cs60364d>.
- (7) Lal, S.; Clare, S. E.; Halas, N. J. Nanoshell-Enabled Photothermal Cancer Therapy: Impending Clinical Impact. *Acc. Chem. Res.* **2008**, *41* (12), 1842.
- (8) Urban, A. S.; Pfeiffer, T.; Fedoruk, M.; Lutich, A. A.; Feldmann, J. Single-Step Injection of Gold Nanoparticles through Phospholipid Membranes. *ACS Nano* **2011**, *5* (5), 3585–3590. <https://doi.org/10.1021/nn201132a>.
- (9) Ghosh, P.; Han, G.; De, M.; Kim, C. K.; Rotello, V. M. Gold Nanoparticles in Delivery Applications. *Adv. Drug Deliv. Rev.* **2008**, *60* (11), 1307–1315. <https://doi.org/10.1016/j.addr.2008.03.016>.
- (10) Baroud, C. N.; Delville, J. P.; Gallaire, F.; Wunenburger, R. Thermocapillary Valve for Droplet Production and Sorting. *Phys. Rev. E - Stat. Nonlinear, Soft Matter Phys.* **2007**, *75* (4), 1–5. <https://doi.org/10.1103/PhysRevE.75.046302>.
- (11) Taylor, A. B.; Siddiquee, A. M.; Chon, J. W. M. Below Melting Point Photothermal Reshaping of Single Gold Nanorods Driven by Surface Diffusion. *ACS Nano* **2014**, *8* (12), 12071–12079. <https://doi.org/10.1021/nn5055283>.
- (12) Petrova, H.; Juste, J. P.; Pastoriza-Santos, I.; Hartland, G. V.; Liz-Marzán, L. M.; Mulvaney, P. On the Temperature Stability of Gold Nanorods: Comparison between Thermal and Ultrafast Laser-Induced Heating. *Phys. Chem. Chem. Phys.* **2006**, *8* (7), 814–821. <https://doi.org/10.1039/b514644e>.
- (13) Baffou, G.; Kreuzer, M. P.; Kulzer, F.; Quidant, R. Temperature Mapping near Plasmonic Nanostructures Using Fluorescence Polarization Anisotropy. *Opt. Express* **2009**, *17* (5), 3291. <https://doi.org/10.1364/oe.17.003291>.
- (14) Baffou, G. Cross-Grating Phase Microscopy for Nanophotonics. **2021**, 1–6.
- (15) Jollans, T.; Calderola, M.; Sivan, Y.; Orrit, M. Effective Electron Temperature Measurement Using Time-Resolved Anti-Stokes Photoluminescence. *J. Phys. Chem. A* **2020**, *124* (34), 6968–6976. <https://doi.org/10.1021/acs.jpca.0c06671>.
- (16) Prins, P. T.; Geitenbeek, R. G.; Meijerink, A. NaYF<sub>4</sub>:Er<sup>3+</sup>/Yb<sup>3+</sup> Nanocrystals for Nanothermometry Exploring Upconversion in NaYF<sub>4</sub>:Er<sup>3+</sup>/Yb<sup>3+</sup> Nanocrystals for Nanothermometry with a Wide Temperature Range. **2016**.
- (17) Jaque, D.; Vetrone, F. Luminescence Nanothermometry. *Nanoscale* **2012**, *4* (15), 4301–4326. <https://doi.org/10.1039/c2nr30764b>.
- (18) Geitenbeek, R. G.; Nieuwelink, A. E.; Jacobs, T. S.; Salzmänn, B. B. V.; Goetze, J.;

- Meijerink, A.; Weckhuysen, B. M. In Situ Luminescence Thermometry to Locally Measure Temperature Gradients during Catalytic Reactions. *ACS Catal.* **2018**, *8* (3), 2397–2401. <https://doi.org/10.1021/acscatal.7b04154>.
- (19) Geitenbeek, R. G.; Prins, P. T.; Albrecht, W.; Van Blaaderen, A.; Weckhuysen, B. M.; Meijerink, A. NaYF<sub>4</sub>:Er<sup>3+</sup>,Yb<sup>3+</sup>/SiO<sub>2</sub> Core/Shell Upconverting Nanocrystals for Luminescence Thermometry up to 900 K. *J. Phys. Chem. C* **2017**, *121* (6), 3503–3510. <https://doi.org/10.1021/acs.jpcc.6b10279>.
- (20) Du, P.; Luo, L.; Yu, J. S. Upconversion Emission, Cathodoluminescence and Temperature Sensing Behaviors of Yb<sup>3+</sup> Ions Sensitized NaY(WO<sub>4</sub>)<sub>2</sub>:Er<sup>3+</sup> Phosphors. *Ceram. Int.* **2016**, *42* (5), 5635–5641. <https://doi.org/10.1016/j.ceramint.2015.12.083>.
- (21) Aiello, C. D.; Pickel, A. D.; Barnard, E.; Wai, R. B.; Monachon, C.; Wong, E.; Aloni, S.; Ogletree, D. F.; Dames, C.; Ginsberg, N. Cathodoluminescence-Based Nanoscopic Thermometry in a Lanthanide-Doped Phosphor. **2018**.
- (22) Mauser, K. W.; Solà-García, M.; Liebrau, M.; Damilano, B.; Coulon, P. M.; Vézian, S.; Shields, P. A.; Meuret, S.; Polman, A. Employing Cathodoluminescence for Nanothermometry and Thermal Transport Measurements in Semiconductor Nanowires. *ACS Nano* **2021**, *15* (7), 11385–11395. <https://doi.org/10.1021/acsnano.1c00850>.
- (23) Stockman, M. I. Nanoplasmonics: The Physics behind the Applications. *Phys. Today* **2011**, *64* (2), 39–44. <https://doi.org/10.1063/1.3554315>.
- (24) Bohren, C. F. How Can a Particle Absorb More than the Light Incident on It? *Am. J. Phys.* **1983**, *51* (4), 323–327. <https://doi.org/10.1119/1.13262>.
- (25) Brongersma, M. L.; Halas, N. J.; Nordlander, P. Plasmon-Induced Hot Carrier Science and Technology. *Nat. Nanotechnol.* **2015**, *10* (1), 25–34. <https://doi.org/10.1038/nnano.2014.311>.
- (26) Mouhot, C.; Villani, C. On Landau Damping. *Acta Math.* **2011**, *207* (1), 29–201. <https://doi.org/10.1007/s11511-011-0068-9>.
- (27) Watanabe, K.; Menzel, D.; Nilius, N.; Freund, H. J. Photochemistry on Metal Nanoparticles. *Chem. Rev.* **2006**, *106* (10), 4301–4320. <https://doi.org/10.1021/cr050167g>.
- (28) Frischorn, C.; Wolf, M. Femtochemistry at Metal Surfaces: Nonadiabatic Reaction Dynamics. *Chem. Rev.* **2006**, *106* (10), 4207–4233. <https://doi.org/10.1021/cr050161r>.
- (29) Jiang, K.; Smith, D. A.; Pinchuk, A. Size-Dependent Photothermal Conversion Efficiencies of Plasmonically Heated Gold Nanoparticles. *J. Phys. Chem. C* **2013**, *117* (51), 27073–27080. <https://doi.org/10.1021/jp409067h>.
- (30) Baffou, G. *Thermoplasmonics: Heating Metal Nanoparticles Using Light*; 2018.
- (31) Baffou, G.; Quidant, R.; García De Abajo, F. J. Nanoscale Control of Optical Heating in Complex Plasmonic Systems. *ACS Nano* **2010**, *4* (2), 709–716. <https://doi.org/10.1021/nn901144d>.
- (32) Bohren, C. F.; Huffman, D. R. Absorption and Scattering by a Sphere. *Absorpt. Scatt. Light by Small Part.* **2007**, 82–129. <https://doi.org/10.1002/9783527618156.ch4>.
- (33) Hohenester, U.; Trügler, A. MNPBEM - A Matlab Toolbox for the Simulation of Plasmonic Nanoparticles. *Comput. Phys. Commun.* **2012**, *183* (2), 370–381. <https://doi.org/10.1016/j.cpc.2011.09.009>.
- (34) Binnemans, K. Lanthanide-Based Luminescent Hybrid Materials. *Chem. Rev.* **2009**, *109* (9), 4283–4374. <https://doi.org/10.1021/cr8003983>.

- (35) Luís Dias Carlos, Fernando Palacio, F. P. P. Thermometry at the Nanoscale: Techniques and Selected Applications.
- (36) Dong, B.; Cao, B.; Feng, Z.; Wang, X.; Li, C.; Hua, R. Up-Conversion Emissions of Er<sup>3+</sup>-Yb<sup>3+</sup> Codoped Al<sub>2</sub>O<sub>3</sub> Nanoparticles by the Arc Discharge Synthesis Method. *Sci. China, Ser. G Physics, Mech. Astron.* **2009**, *52* (7), 1043–1046. <https://doi.org/10.1007/s11433-009-0132-z>.
- (37) Lu, D.; Mao, C.; Cho, S. K.; Ahn, S.; Park, W. Experimental Demonstration of Plasmon Enhanced Energy Transfer Rate in NaYF<sub>4</sub>:Yb<sup>3+</sup>,Er<sup>3+</sup> Upconversion Nanoparticles. *Sci. Rep.* **2016**, *6* (November 2015), 1–11. <https://doi.org/10.1038/srep18894>.
- (38) Förster, T. 10th Spiers Memorial Lecture. Transfer Mechanisms of Electronic Excitation. *Discuss. Faraday Soc.* **1959**, *27* (10), 7–17. <https://doi.org/10.1039/DF9592700007>.
- (39) Suyver, J. F.; Grimm, J.; Krämer, K. W.; Güdel, H. U. Highly Efficient Near-Infrared to Visible up-Conversion Process in NaYF<sub>4</sub>:Er<sup>3+</sup>,Yb<sup>3+</sup>. *J. Lumin.* **2005**, *114* (1), 53–59. <https://doi.org/10.1016/j.jlumin.2004.11.012>.
- (40) Guo, Q.; Xu, M.; Yuan, Y.; Gu, R.; Yao, J. Self-Assembled Large-Scale Monolayer of Au Nanoparticles at the Air/Water Interface Used as a SERS Substrate. *Langmuir* **2016**, *32* (18), 4530–4537. <https://doi.org/10.1021/acs.langmuir.5b04393>.
- (41) Van Swieten, T. P.; Van Omme, T.; Van Den Heuvel, D. J.; Vonk, S. J. W.; Spruit, R. G.; Meirer, F.; Garza, H. H. P.; Weckhuysen, B. M.; Meijerink, A.; Rabouw, F. T.; Geitenbeek, R. G. Mapping Elevated Temperatures with a Micrometer Resolution Using the Luminescence of Chemically Stable Upconversion Nanoparticles. *ACS Appl. Nano Mater.* **2021**, *4* (4), 4208–4215. <https://doi.org/10.1021/acsnm.1c00657>.
- (42) Kaiser, M.; Würth, C.; Kraft, M.; Hyppänen, I.; Soukka, T.; Resch-Genger, U. Power-Dependent Upconversion Quantum Yield of NaYF<sub>4</sub>:Yb<sup>3+</sup>,Er<sup>3+</sup> Nano- and Micrometer-Sized Particles-Measurements and Simulations. *Nanoscale* **2017**, *9* (28), 10051–10058. <https://doi.org/10.1039/c7nr02449e>.

## Appendix

### 1 - Particle analyser + script

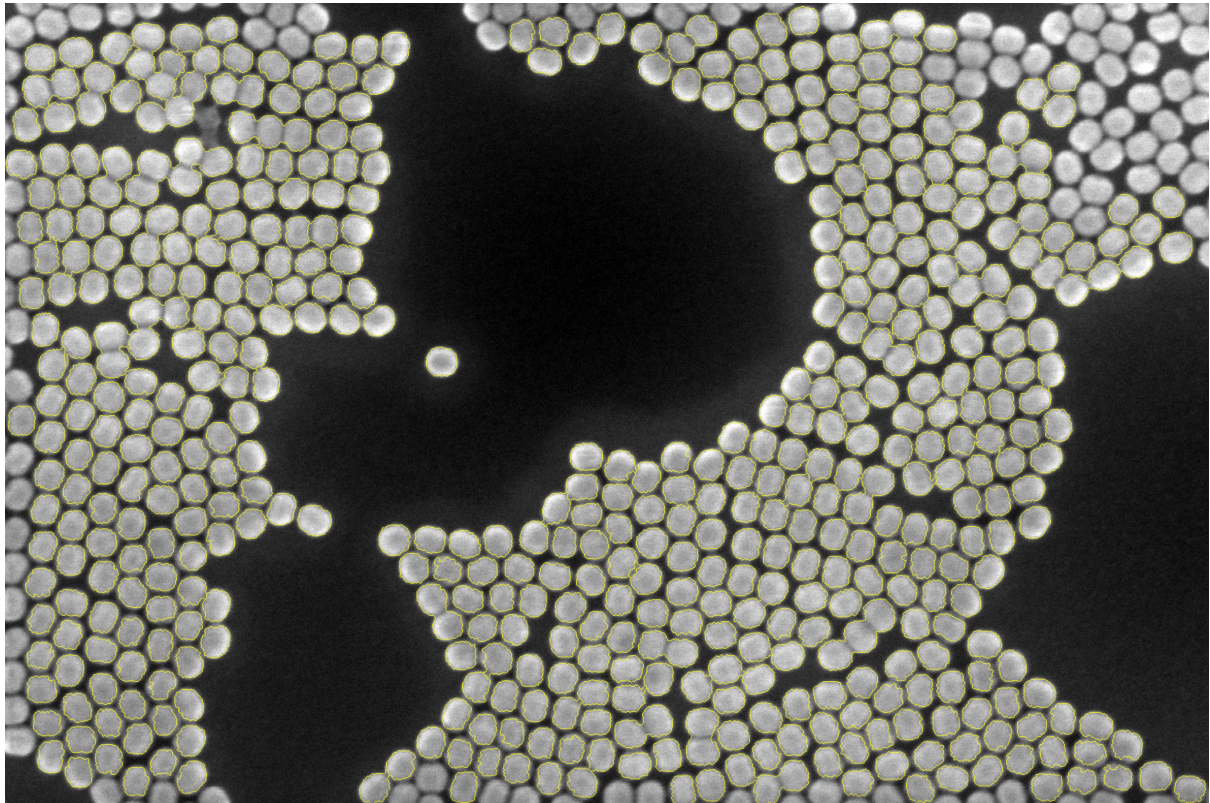


Figure 23: Example of the particle analyser used for determining the particle size distribution of the nanoparticles.

```
import os
import cv2.cv2
import numpy as np
import matplotlib.pyplot as plt
import cv2
from skimage import io, color, measure
from skimage.segmentation import clear_border
import pandas as pd
import scipy
from scipy.optimize import curve_fit, OptimizeWarning
from scipy import ndimage
import warnings
import matplotlib.cm as cm
import math
from time import sleep
from tqdm import tqdm
from pytesseract import pytesseract
from General_Functions_Tjom import (makeplot, give_index, Peak_Fit,
Lorentzian, Gaussian, Rename_Columns, analyse_particles)

os.chdir("/Users/tjomarens/Desktop/Stage Amolf/SEM Images/For report/")

pd.set_option('display.max_columns', None)

path_to_tesseract = r"/opt/homebrew/bin/tesseract"
pytesseract.tesseract_cmd = path_to_tesseract

np.set_printoptions(threshold=np.inf)
Input_Folder = r"/Users/tjomarens/Desktop/Stage Amolf/SEM Images/For
```

```

report/"
File_Name =
"TA211125_SC2_50uL(50x,3000rpm)_AuNR_RER6_100uL(5x,3000rpm)_NaYF4_Si_center
_006 1.tif"

#print(analyse_particles(Input_Folder+File_Name, 10, 1, 1, 0.3,
Show_Image=True, Show_Hist=True))

img = cv2.imread(Input_Folder + File_Name, 0)
meta_data = img[1023:1065, 1056:1534]
img = img[:1023, :]

meta_data_text = '500 nm'
#meta_data_text = pytesseract.image_to_string(meta_data)
numbers = [int(word) for word in meta_data_text.split() if word.isdigit()]
meter = [word for word in meta_data_text.split() if 'm' in word]
meta_data = meta_data[2:-2, :]

print(numbers, meter)

meta_data[meta_data < 100] = 0
meta_data[meta_data > 50] = 255
cv2.imshow("Overlay on original image", meta_data)
cv2.waitKey(0)
scale_bar = np.where(meta_data == 255)
length = scale_bar[1].max() - scale_bar[1].min()

pixel_length = [numbers[0] / length, str(*meter)]

#cv2.imshow("Overlay on original image", meta_data[:, 100:380])
#cv2.waitKey(0)

img1 = cv2.imread(Input_Folder + File_Name)

img1 = img1[:1023, :]
#ret, thresh = cv2.threshold(img, 0, 255,
cv2.THRESH_BINARY+cv2.THRESH_OTSU)

#img[img > 55] = 255
img[img < 50] = 0
thresh = img

kernel = np.ones((3, 3), np.uint8)

opening = cv2.morphologyEx(thresh, cv2.MORPH_OPEN, kernel, iterations=1)
closing = cv2.morphologyEx(opening, cv2.MORPH_CLOSE, kernel, iterations=1)
opening = clear_border(opening)
cv2.imshow("Overlay on original image", opening)
cv2.waitKey(0)

sure_bg = cv2.dilate(opening, kernel, iterations=1)

dist_transform = cv2.distanceTransform(opening, cv2.DIST_L2, 3)
ret2, sure_fg = cv2.threshold(dist_transform, 0.4 * dist_transform.max(),
255, 0)
sure_fg = np.uint8(sure_fg)

unknown = cv2.subtract(sure_bg, sure_fg)
ret3, markers = cv2.cv2.connectedComponents(sure_fg)

```

```

markers = markers + 1
markers[unknown == 255] = 0

markers = cv2.watershed(img1, markers)

img1[markers == -1] = [0, 255, 255]
img2 = color.label2rgb(markers, bg_label=0)

props = measure.regionprops_table(markers, properties=('area',
'equivalent_diameter', 'orientation',
'major_axis_length',
'minor_axis_length'))

df = pd.DataFrame(props)
df = df.iloc[1:, :]
df['aspect_ratio'] = round(df['major_axis_length']/df['minor_axis_length'],
1)
pixels_to_squared = ['area']
pixels_to_distance = ['equivalent_diameter', 'major_axis_length',
'minor_axis_length']

for prop in df.columns:
    if prop in pixels_to_squared:
        df[str(prop)] = df[str(prop)].apply(lambda x: x *
pixel_length[0]**2)
        #df = df.rename(columns={str(prop): str(prop) +
'({}\u00b2)'.format(pixel_length[1])})

    if prop in pixels_to_distance:
        df[str(prop)] = df[str(prop)].apply(lambda x: x * pixel_length[0])
        #df = df.rename(columns={str(prop): str(prop) +
'({})'.format(pixel_length[1])})

cv2.imshow("Overlay on original image", img1)
cv2.imshow("Colored Grains", img2)
cv2.waitKey(0)

Aspect_Boundaries = [0.8, 3.5]
Length_Boundaries = [0, 40]
Width_Boundaries = [10, 30]
df = df[(df.aspect_ratio > Aspect_Boundaries[0]) & (df.aspect_ratio <
Aspect_Boundaries[1])]
#df = df[(df.major_axis_length > Length_Boundaries[0]) &
(df.major_axis_length < Length_Boundaries[1])]
#df = df[(df.minor_axis_length > Width_Boundaries[0]) &
(df.minor_axis_length < Width_Boundaries[1])]
print(df)

#df.to_excel('rods_outer.xlsx')

font = {'size' : 16}

plt.rc('font', **font)

plt.hist(x=df['aspect_ratio'], bins='auto', color='#0504aa',
alpha=0.7, rwidth=0.85)
plt.xlabel('Aspect ratio (nm)')
plt.ylabel('Counts')
plt.show()

```



## 2 - Effect of overlapping $^2H_{9/2}$ and $^4S_{3/2}$ emission

During an experiment with only thermometer particles and upon 980 nm illumination, the effect of overlap between the  $^2H_{9/2}$  and  $^4S_{3/2}$  emission was clearly observed as the LIR first increased and then stabilized upon moving away from the middle of the illumination spot (Fig. 8b).

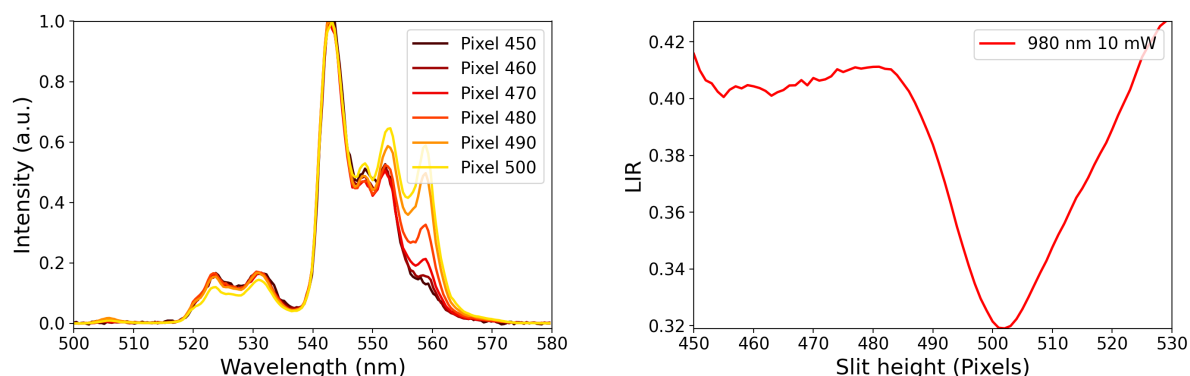


Figure 24: a) Luminescence emission spectra of Erbium for several positions with regard to the middle of the excitation beam upon illumination with a 980 nm laser at 10 mw. b) The luminescence intensity peak ratio plotted versus the pixels in the slit. The peak ratio close to focus of the beam is low due to a strong tail, originating from the  $^2H_{9/2}$  level, under the 540 nm peak, this effect diminishes as the  $^2H_{9/2}$  peak intensity decreases till eventually the peak ratio flattens.

This is opposite to what you would expect from heating by the laser. The emission spectra show the origin of this observation as the measurements closer to middle of the spot have a higher relative intensity for the peaks between 550 and 560 nm (Fig. 8a). Therefore, due to the more intense 980 nm illumination in the middle of the beam the three-photon up conversion process was higher.<sup>41</sup> Furthermore, the relative peak intensity of the peaks at 530 nm moved in opposite direction as they are less intense in the middle of the beam. The tail of the  $^2H_{9/2}$  emission most likely reached under the peak at 545 nm resulting in a relative decrease of the peaks at 530 nm. This significant  $^2H_{9/2}$  emission thus affected the temperature calculations and introduced a systematic error to the system. Van Swieten et al. corrected their data by using a microcrystalline  $NaYF_4:Er^{3+},Yb^{3+}$  reference spectrum to subtract from the data to determine the shape of the  $^2H_{9/2}$  emission and then used a linear fit to determine its contribution in each spectrum.<sup>41</sup> However, in this case this is not a viable method because the  $^2H_{9/2}$  emission tail reaches under the 540 nm peak. Therefore, the 980 nm excitation power needs to be kept low to minimize the effect of this overlap.

### 3 - Electron penetration depth simulations (Casino) 1 keV

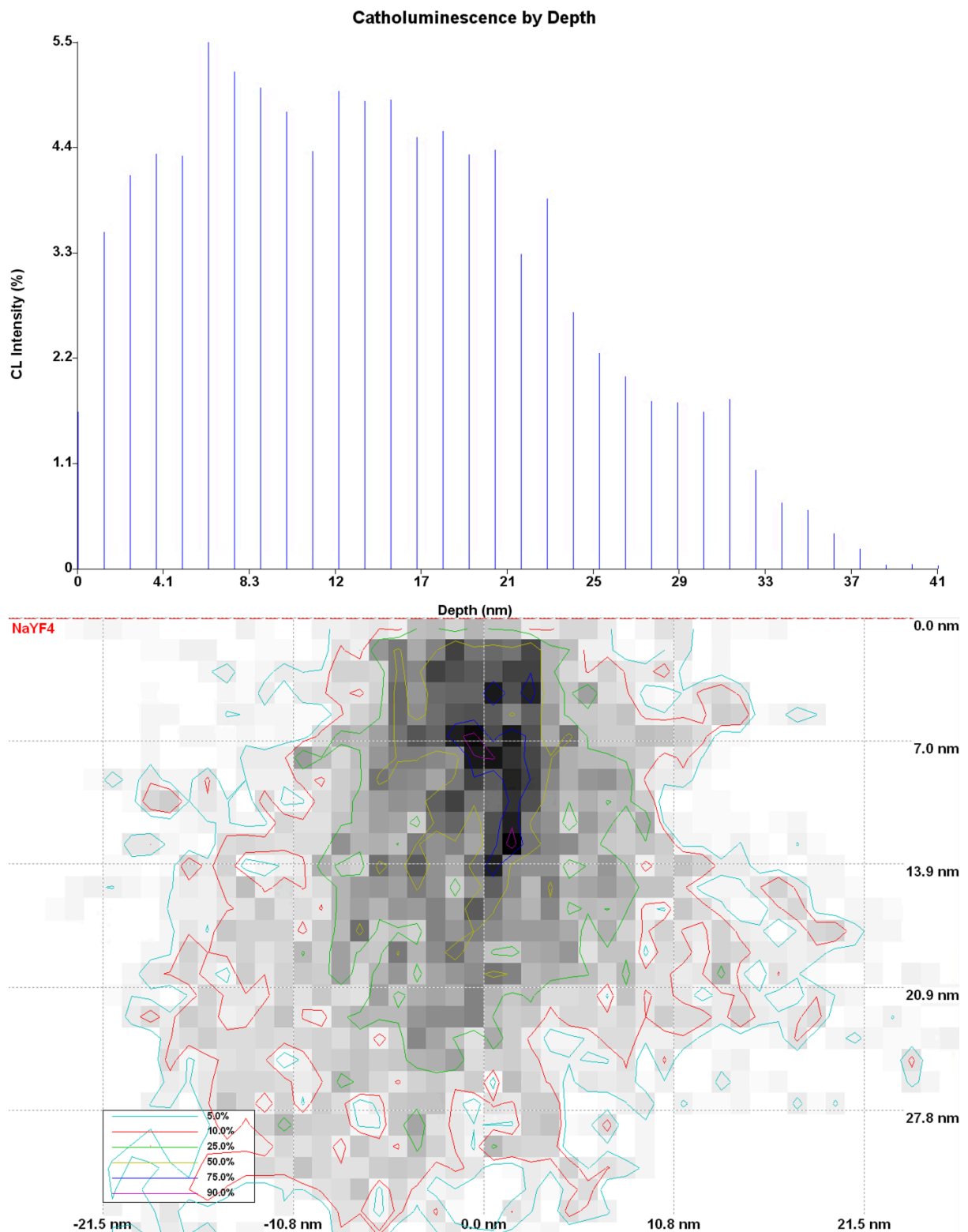


Figure 25: a) CL signal by depth in the sample for acceleration voltage of 1 keV b) simulation result calculated with CASINO. Electrons have a penetration depth of approximately 40 nm at 1 keV.

5 keV

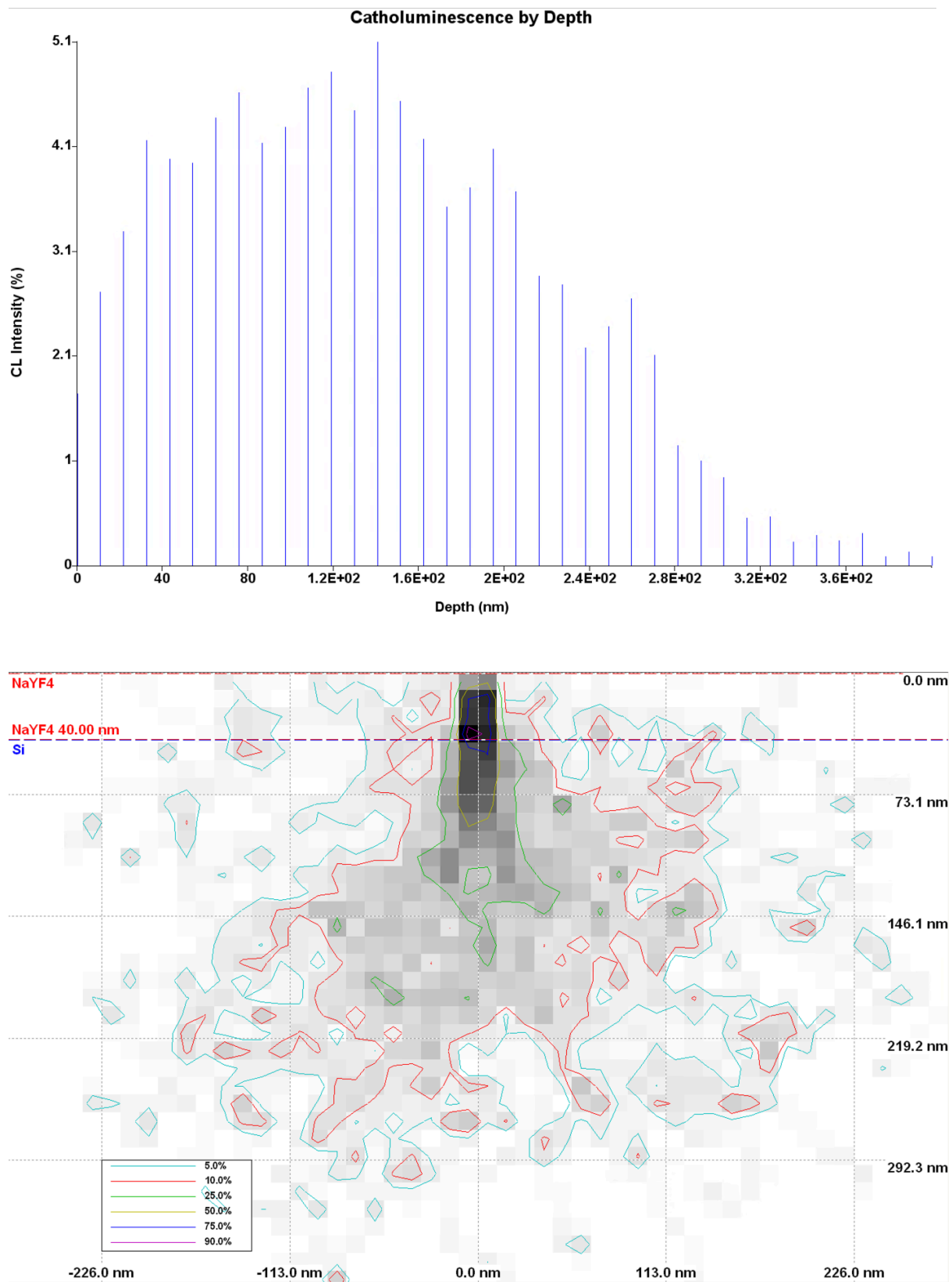


Figure 26: a) CL signal by depth in the sample for acceleration voltage of 5 keV b) simulation result calculated with CASINO. Electrons have a penetration depth of approximately 360 nm at 5 keV.

10 keV

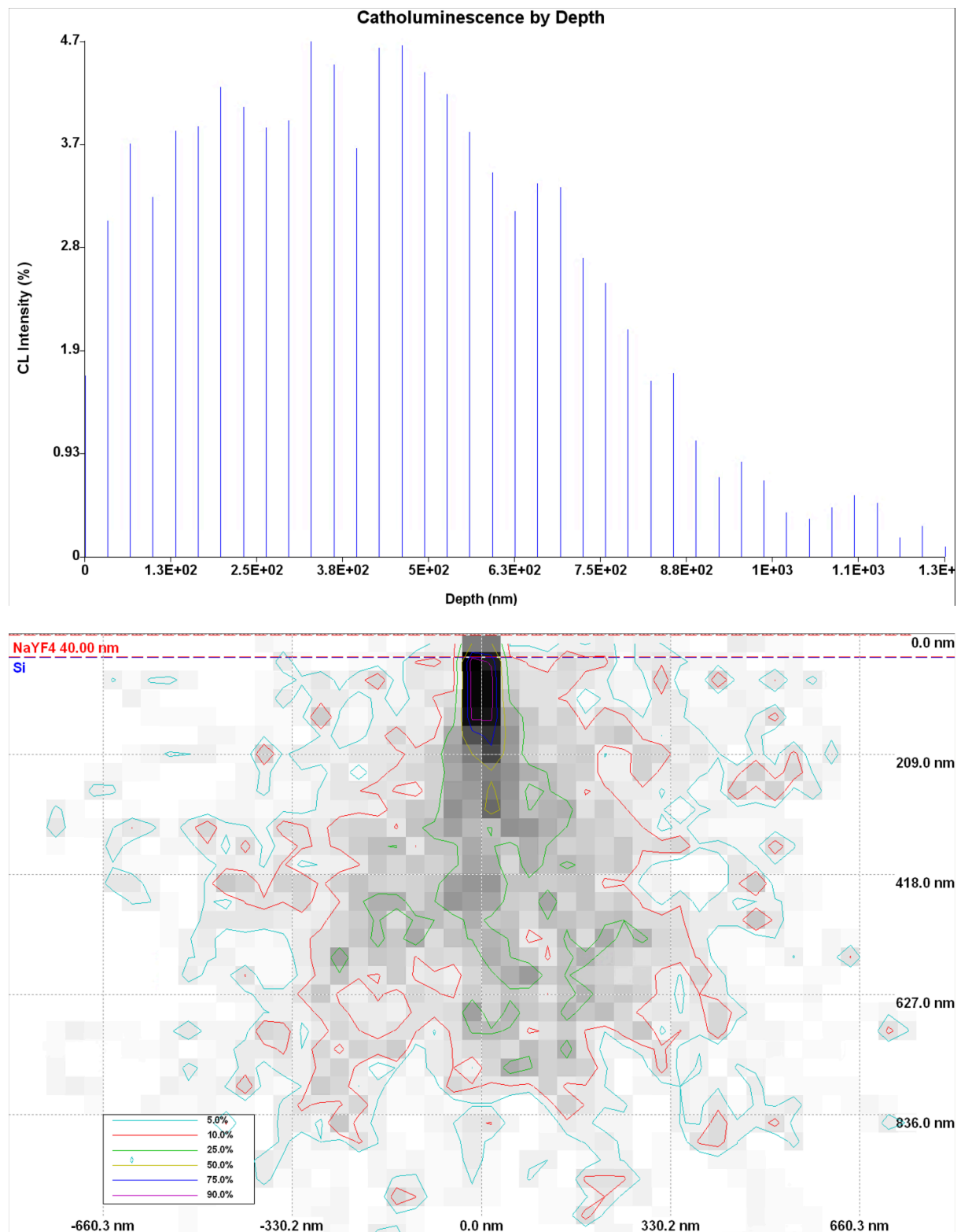


Figure 27: a) CL signal by depth in the sample for acceleration voltage of 10 keV b) simulation result calculated with CASINO. Electrons have a penetration depth of approximately 1300 nm at 10 keV.